12-1-2017

Probing Broad Line Regions of Active Galactic Nuclei

Champika Sandamali Weerasooriya
University of Nevada, Las Vegas, sanduwee@gmail.com

PROBING BROAD LINE REGIONS OF ACTIVE GALACTIC NUCLEI

by

Champika Sandamali Weerasooriya

Bachelor of Science – Physics
University of Peradeniya, Sri Lanka
2007

Master of Science – Physics
University of Kentucky, Lexington
2012

A dissertation submitted in partial fulfillment
of the requirements for the

Doctor of Philosophy – Astronomy

Department of Physics and Astronomy

College of Sciences

The Graduate College

University of Nevada, Las Vegas

December 2017

UNLV | GRADUATE COLLEGE

Dissertation Approval

The Graduate College
The University of Nevada, Las Vegas

November 13, 2017

This dissertation prepared by

Champika Sandamali Weerasooriya

entitled

Probing Broad Line Regions of Active Galactic Nuclei

is approved in partial fulfillment of the requirements for the degree of

Doctor of Philosophy – Astronomy
Department of Physics and Astronomy

George Rhee, Ph.D.
Examination Committee Chair

Kathryn Hausbeck Korgan, Ph.D.
Graduate College Interim Dean

Daniel Proga, Ph.D.
Examination Committee Member

Stephen Lepp, Ph.D.
Examination Committee Member

David Lee, Ph.D.
Graduate College Faculty Representative

Abstract

Probing Broad Line Regions of Active Galactic Nuclei

by

Champika Sandamali Weerasooriya

Dr. George Rhee, Examination Committee Chair

Professor of Physics

University of Nevada, Las Vegas

The broad line regions (BLR) of Type I Active galactic nuclei (AGN) are too small to be spatially resolved even with the most powerful telescopes available. Observations suggest that BLR gas is moving under the influence of the gravitational potential of the central super massive black-hole (SMBH) and responds to the variations in the ionizing continuum flux of the accretion disk, giving rise to broad emission line variations with a time delay. Reverberation mapping campaigns seek to use this time variability to resolve the BLRs in the time domain instead of spatial domain, providing a way to infer geometry and kinematics of the BLR and calculate the mass of the SMBH. Numerous BLR models have been proposed over the years but only few of them are physically motivated. In this work, we examine the feasibility of constraining the parameters of such a physically motivated model; a disk-wind model of the BLR. We employ a Bayesian inference framework to compare predicted line light curves to an observed line light curve, using simulated data. A shortcoming of reverberation mapped data is that they may contain large gaps between consecutive observations. Therefore, additionally, we implement a method and provide a code to evenly sample real observed continuum light curves in order to carry out similar analysis using real observational data.

Acknowledgements

First and foremost, I would like to thank my advisor Dr. George Rhee for his continued support and guidance during my time at UNLV. I am grateful for the numerous times he has encouraged and pushed me to do better. Without his constant encouragement, I would not have been able to face the qualifying exam - which was a crucial step towards my doctorate - in my very first semester at UNLV before taking any preparatory courses, and get through it successfully. Most of the knowledge I have acquired in statistical methods while working on my project, I owe to him. Whenever I had difficulty grasping those concepts, he explained them to me beautifully, greatly reducing the steepness of my learning curve.

Dr. Daniel Proga is the next person I would like to thank in the long list of people to whom I owe my gratitude. It is with him I took my very first Astrophysics course at UNLV, which I enjoyed very much. He was available to discuss concepts not just related to the course, but outside of it as well be it Saturns hexagon or streamlined water arches at Bellagio conservatory. I admire his willingness to work to get to the bottom of a problem no matter how difficult and/or time consuming it is. Also, I have benefitted a lot from his expertise in all things AGN, while working on this project.

I thank Dr. David Lee and Dr. Stephen Lepp for serving in my advisory committee. It is from Dr. Lepp that I learned not to underestimate the power of telling people what they already know when doing presentations, valuable advice which has served me well since.

When I walked into the Astrophysics I class in Fall 2013, I was fully prepared (quite egotistically) not to gain a whole lot of new knowledge, having studied the textbook myself the semester before. What stunned me by the end of the semester was how deep an understanding I gained during the course, which was sobering. Dr. Bing Zhang, I thank you for being an outstanding teacher.

To my colleagues at the Department of Physics and Astronomy who have contributed to make my time at UNLV a pleasant and fruitful one; be it a kind word, friendship, or a helping hand, I thank you all sincerely. I want to thank my colleague, collaborator, and, newly minted graduate Dr.

Timothy Waters specifically, for without his contribution this work would not have been possible.
I owe my thanks to Dr. Matt Pedersen for maintaining a LaTeX style file for UNLV and his assistance in formatting the template to suit the Department of Physics & Astronomy.
Gail, I want to thank you specially for helping me out when I was still new in Las Vegas and was facing a very unnerving situation. I appreciate it very much.
Finally, I want to thank my family for loving me and for being there for me unconditionally. Specially, I want to thank my loving husband Sach, for being there for me through thick and thin and for supporting me in everything I do and aspire to do.
Thank you all!

Champika Sandamali Weerasooriya

University of Nevada, Las Vegas

December 2017

Table of Contents

List of Tables

List of Figures

List of Algorithms

Chapter 1

Introduction

One of the fundamental questions in Astronomy is understanding the origin and evolution of galaxies. Supermassive black-holes (SMBH) in the centers of galaxies play a key role in galactic formation and evolution. It is thus imperative to probe the nuclear region of these galaxies and to measure the mass of the black-holes (M_{BH}) in order to further the efforts to answer this important question.

1.1 Active vs Quiescent galaxies

Depending on the amount of activity exhibited by galaxies, measured using factors such as the rate of star formation or the amount of luminosity of the central compact region, they could be categorized as either quiescent or active galaxies. Quiescent galaxies such as our own Milky Way are more abundant in the local universe. As the name suggests, they do not display unusual activities and are believed to contain dormant SMBHs in their centers which have already passed the growing phase. Contrastingly, central compact regions of active galaxies named active galactic nuclei (AGN) house SMBHs that are actively growing by amassing matter through accretion disks. In the process the accretion disks emit enormous amounts of radiation often outshining their host galaxies, over a broad wavelength range in the electromagnetic spectrum. In addition, AGN are thought to have several other components as well, such as a broad line emitting region in the immediate vicinity of the accretion disk, a dusty torus, a narrow line emitting region farther away, etc.

Historically, AGN have been classified into numerous subgroups according to their observed properties. Members of the AGN family easily span nine orders of magnitude in luminosity, from not so bright Low-luminosity Active Galaxies to extremely luminous Quasars. Furthermore, some of them are observed to be emitting strong and broad ultra-violet (UV) and optical emission lines.

Many quiescent galaxies are sufficiently close to the earth so that their central regions can be directly observed and M_{BH} can be measured using stellar and gas dynamics (McConnell & Ma (2013)). However, most active galaxies are too far away. Therefore, their nuclear compact regions are too small in angular size to be spatially resolved even with the most powerful telescopes available. Thus, making similar measurements required to make any meaningful inferences about the central region is impossible. For AGN which display broad emission lines in their spectra, their time variability can be used to resolve the central region temporally rather than spatially. Reverberation Mapping technique introduced by Blandford & McKee (1982) employs time variability in emission line fluxes and AGN continuum fluxes to explore the broad emission line region of AGN, and, provides a pathway to calculate the mass of the central supermassive black-hole.

1.2 Outline

In this dissertation, Chapter 2 is dedicated to discussing what is known so far about the broad line region. Chapter 3 describes the theory of reverberation mapping technique and their general results. Next, we discuss some models that have been proposed as candidates for BLR structure in Chapter 4. Chapter 5 explores a physically motivated BLR model, specifically exploring the feasibility of constraining model parameters. Finally, we discuss constrained random fields and how this is applied to interpolate and extrapolate AGN continuum light curves in Chapter 6.

Chapter 2

Broad Line Region

Strong and broad UV and optical emission lines are characteristic of Type I AGN spectra. The region where they originate is named the broad line region, although the exact nature of this region still remains a mystery. The BLR is thought to be at a distance ~ 1000 r_g (e.g.; Peterson (2008); Schimoia et al. (2017)) from the central source, which makes the BLR highly exposed to strong radiation.

2.1 Line emitting Gas

Relative strengths of the observed broad emission lines indicate that they are not thermally ionized, rather photoionized by the intense radiation from the central source. When AGN ionizing radiation of wavelengths < 912 Å incident upon BLR gas, the gas is ionized then recombines, giving rise to broad emission lines. When the rate of photoionization is balanced by the rate of recombination, photoionization equilibrium is reached. Provided the photoionization equilibrium conditions, an *ionization parameter* U can be defined, and is given by,

$$U = \frac{Q_{\rm ion}({\rm H})}{4\pi r^2 c n_e} \tag{2.1}$$

Here, $Q_{ion}(H)$ is the rate of H-ionizing photon emission (s^{-1}) of the continuum source.

$$Q_{\rm ion}({\rm H}) = \int \frac{L_v}{hv}\, dv \tag{2.2}$$

where, L_ν - specific luminosity of the ionizing source.

Ionization parameter is the ratio of ionizing photon density to gas density and thus indicative of the level of ionization of the gas. Therefore, in the context of BLR gas, it is important to compute this parameter.

The BLR gas is estimated to be in photoionization equilibrium at a temperature $\sim 10^4$ K. In the context of optically thin BLR gas, it is important to compute this ionization parameter . This reinforces the fact that thermal broadening can not be responsible for the broad emission lines since at $T = 10^4$ K, thermal widths of the lines will be ~ 10 km s^{-1}.

Estimations suggest $U \sim 10^{-2}$ (e.g., Ferland & Mushotzky (1982)), meaning only the irradiated surfaces of the BLR clouds are subjected to a high level of ionization (see section 7.1 in Netzer (2013)). The most abundant ions in the ionized parts of BLR are He II-III, O IV-VI, C III-IV, predicting strong permitted emission lines Hα, Lyα, C IVλ1549, and, O VIλ1035. Due to the high column density $\sim 10^{23}$ cm^{-2} of BLR, a significant portion of BLR clouds remain neutral or at a level of low ionization. Predicted strong lines for these portions are H I, Mg II, and Fe II. Figure 2.1 shows a composite spectrum of several quasars containing many emission lines.

The observed emission lines appear to be kinematically composite; composed of a broad component and a narrow component. Only broad components of the lines originate in the BLR. They display Doppler widths of about 1000 km s^{-1} – 25000 km s^{-1}. Very high Doppler widths indicate that broad emission lines originate very deep in the gravitational potential well of the central SMBH suggesting broad emission lines are a crucial key in probing the nuclear regions of AGN. From strengths of certain density sensitive emission lines, it is determined that broad lines originate in environments where the gas density is $\sim 10^9 - 10^{11}$ cm^{-3}. Observations have shown that permitted lines originate in high density regions of $\sim 10^{11}$ cm^{-3} (Peterson (1993)) while the absence of strong, broad forbidden lines suggests that the BLR has to be at least as dense as $\sim 10^8$ cm^{-3}. The presence of semiforbidden lines such as O III] and C III] indicate the existence of slightly lower density regions of $\sim 10^9$ cm^{-3}.

Narrow components display Doppler widths < 900 km s^{-1} which are much less than those of broad components suggesting that the narrow lines originate much farther away from the BLR. Narrow line component of the spectra contain forbidden lines as well. Therefore, they are assumed to be originating at a low density region $\sim 10^3$ cm^{-3} called Narrow line region (NLR).

Line widths of both broad emission lines and narrow emission lines being much larger than thermal widths (i.e. ~ 10 km s^{-1}) indicate broadening is due to supersonic bulk motions in both cases. Observed equivalent widths, which is a measure of how strong the emission lines are compared to the continuum emission, are $\sim 10 - 100$ Å. Moreover, they imply a global covering factor of about $\sim 10\% - 20\%$ (e.g., Korista & Goad (2000). This means the responding BLR gas clouds cover a small fraction of the solid angle of the central source and allow us to neglect the effects of radiation

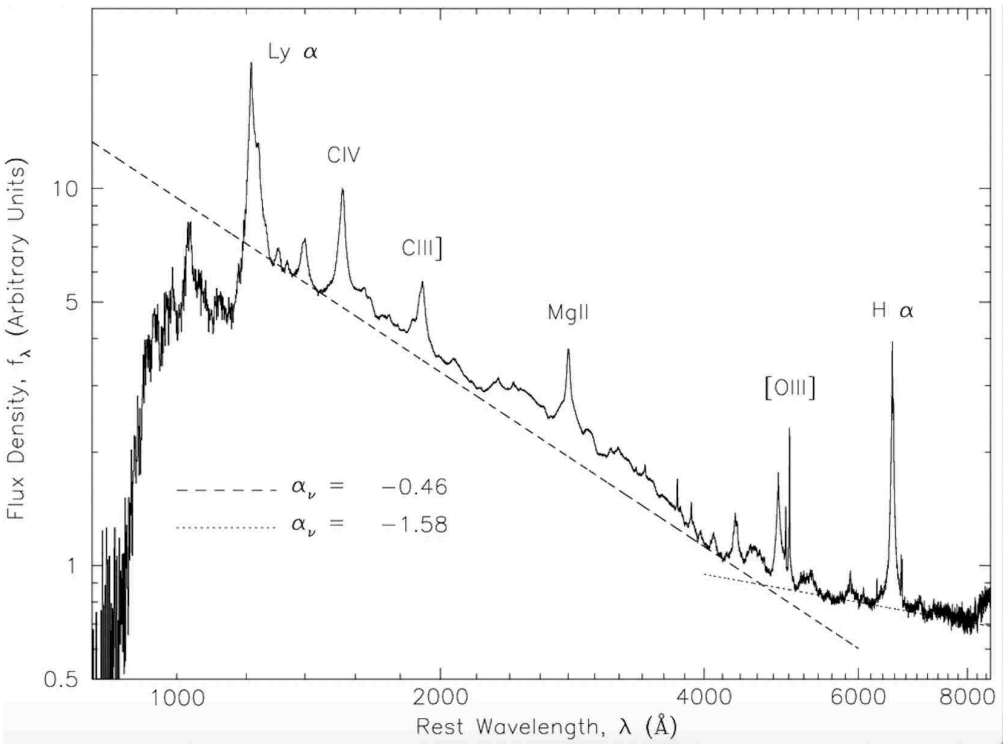

Figure 2.1: A composite quasar spectrum generated using median combining which show broad and narrow emission lines. Power-law fits to the estimated continuum flux are shown in dashed lines. Courtesy Vanden Berk et al. (2001).

emitted by clouds on one another.

Determining the abundances of BLR gas is not easy. But the current inferred values indicate that they are same as solar abundances or sometimes a little higher (e.g., Shields (1976); Hamann & Ferland (1999)). This holds true even for BLR of AGN at high redshifts.

2.2 Basic Variability Properties

Broad emission lines are observed to vary in response to AGN continuum variations with a time delay of days to months. The delay is thought to be due to the light travel time from continuum source to the BLR gas. This leads to the idea of *reverberation mapping* which uses the time lag between the continuum and emission lines to probe Type I AGN BLRs. Reverberation time lags provide a way to measure BLR size.Narrow emission lines do not vary in short time scales as broad lines. But they may vary in much larger time scales.

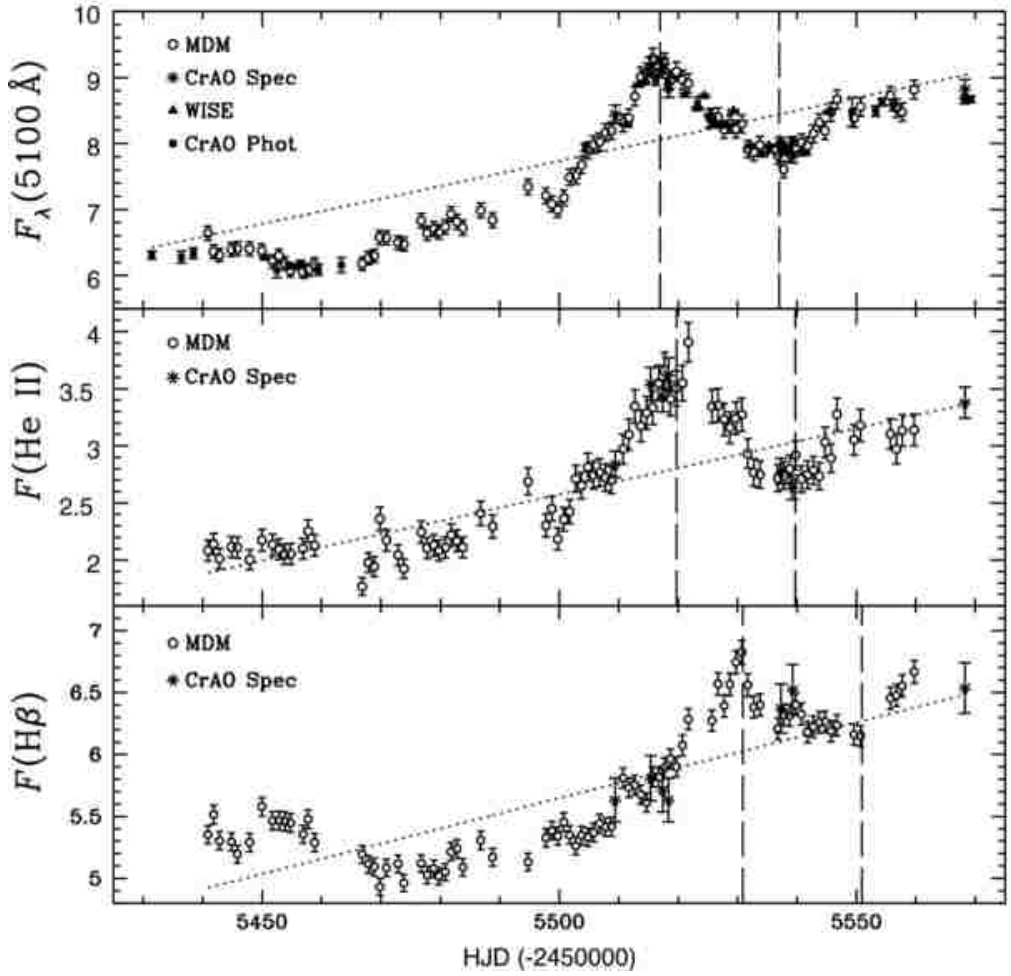

Figure 2.2: Light curves for Mrk 335 showing broad lines lag the continuum.
Top to bottom panels show continuum, He II and Hβ fluxes. Two vertical dashed lines identify the maximum and a local minimum in each panel respectively. He II and Hβ lag the continuum by 2.7 days and 13.9 days respectively. Courtesy Grier et al. (2012a).

2.3 Broad Line Profiles

Gas kinematics of BLR are best understood by studying the line profiles. A variety of different phenomena such as inflows, outflows, Doppler motions, rotation, shocks, and, turbulence can give rise to different line profile shapes. Gaussian line profiles can arise from the Doppler motion of the BLR gas in the gravitational potential of the SMBH (e.g., Peterson & Wandel (1999); Fromerth & Melia (2000); Peterson & Wandel (2000)). Logarithmic line profiles, which explain emission line wings well, could be a result of outflows (e.g., Blumenthal & Mathews (1975); Netzer (1990)). Lorentzian line profiles may arise due to emission from extended accretion disks (e.g., Véron-Cetty et al. (2001); Sulentic et al. (2002); Goad et al. (2012)). However, attempts at fitting line profiles

using simple models do not constrain BLR kinematics in general due to modeling degeneracies. Multi-component Gaussians, a combined model of a Gaussian and a Lorentzian, and, power-law fitting have been tried with success (Netzer (2013). Higher ionization lines tend to be broader indicating that the BLR must be radially stratified.

Chapter 3

Reverberation Mapping

Not long after the discovery of quasars in 1963, variability in optical continuum luminosity was established as a defining characteristic of quasars (Burbidge (1967)). Evidence of emission line flux variability followed soon (Andrillat & Souffrin (1968); Pastoriza & Gerola (1970); Collin-Souffrin et al. (1973); Tohline & Osterbrock (1976)), although measurements were quite crude and showed only major changes like the difference between Type 1 and Type 2 objects with the available technology at the time. Advancements in electronic detectors in 1980s paved the way to establish a strong correlation between AGN continuum and emission line variations (Peterson et al. (1983); Antonucci & Cohen (1983); Ulrich et al. (1991)). The usual trend is, a sudden burst or dip in the observed UV-optical continuum luminosity will be followed by a corresponding burst or dip in broad emission line luminosity after a time delay. The BLR size predicted by the photoionization theory was an order of magnitude larger than the size that was inferred by the initial results, raising concerns over the validity of these results (Peterson et al. (1985)). However, this discrepancy turned out to be due to an oversimplification in the theory (Clavel et al. (1991)). The idea behind the reverberation mapping was first proposed by Bahcall et al. (1972) and Blandford & McKee (1982) explained its theoretical foundation and coined the term *reverberation mapping*. This has become a leading method to explore nuclear regions of Type I AGN providing a way to determine the structure and kinematics of the BLR as well as the black hole mass (Peterson (1993); Peterson et al. (2004)).

The beauty of this technique is that it provides a powerful tool to study black holes over a range of masses and red shifts without requiring to spatially resolve the gravitational sphere of influence of the black hole (Peterson et al. (2004); Woo et al. (2007); Bentz et al. (2009); Denney et al. (2009); Grier et al. (2017)). The principle behind reverberation mapping technique is equivalent to that of

radar technology used in weather mapping. Both use the idea that the structure and kinematics of a system can be inferred from its Doppler-shifted, time-delayed response to an input signal. It so happens that in this case the input signal is produced by the AGN accretion disk in the form of an ionizing continuum. Gas in the BLR responds by undergoing photoionization and emitting broad emission lines with a time lag of days to weeks in the process.

3.1 Reverberation Mapping Theory

In developing reverberation mapping theory, we make several simplifying assumptions based on observations. (Blandford & McKee (1982); Peterson (1993); Peterson (2001); Courvoisier & Clavel (1991); Clavel et al. (1991))

3.1.1 Assumptions

1. The most important time scale is the light travel time across BLR (i.e. reverberation time scale):
$\tau_{\rm rec} << \tau_{\rm rev} << \tau_{\rm dyn}$
Here,
$\tau_{\rm rec} = ({\rm n_e}\alpha_{\rm B})^{-1} \approx 0.1(10^{10}\ {\rm cm^{-3}}/{\rm n_e})$hours - recombination time scale.
$\tau_{\rm rev} \sim {\rm R_{BLR}}/\Delta{\rm V}$ days - reverberation time scale.
$\tau_{\rm dyn} \sim {\rm R_{BLR}}/{\rm c}$ years - dynamical time scale.
where, $\rm n_e$ is the particle density, $({\rm n_e}\alpha_{\rm B})^{-1}$ is the Hydrogen case B recombination coefficient, $\rm R_{BLR}$ is radius of the BLR, and, ΔV is the RMS line width.
We assume that BLR gas respond to continuum variations without any time delay (i.e. recombination time $\tau_{\rm rec}$ is much smaller than light crossing time $\tau_{\rm rev}$). The BLR gas densities are sufficiently high ($\rm n_e \sim 10^9 - 10^{11}\ cm^{-3}$) to validate this assumption.
We also assume that the BLR structure and kinematics do not vary over the course of a reverberation mapping campaign, which may last several months. (i.e. dynamical time scale $\tau_{\rm dyn}$ is much longer than the reverberation time scale $\tau_{\rm rev}$). For Seyferts, $\tau_{\rm dyn} \sim 3 - 5$ years.

2. The continuum is emitted from a point source though not necessarily isotropically:
i.e. the size of the continuum source is much smaller ($\sim 10^{13} - 10^{14}$ cm for Seyferts) than that of the BLR ($\sim 10^{16}$ cm).

3. There is a simple but not necessarily linear or instantaneous relationship between the ionizing continuum variations ($\lambda < 912$ Å) and observed continuum variations:
Reverberation mapping campaigns usually use $\lambda \sim 5100$ Å as a proxy for ionizing continuum under this assumption because majority of the campaigns which have been carried out so far are in optical wavelengths. The success of these campaigns justifies the assumption.

3.1.2 The Transfer Function

With the above assumptions a simple relation between continuum and line variations can be written as,

$$\Delta L(v,t) = \int_0^\infty \Psi(v,\tau_d)\ \Delta C(t-\tau_d)\, d\tau_d \tag{3.1}$$

where, $\Delta L(v,t)$ and $\Delta C(t)$ are variable parts of the velocity-resolved emission line light curve and observed continuum light curve respectively. Here, τ_d is the time delay and $\Psi(v,\tau_d)$ is known as the *2D transfer function*. It is also called the *echo image* or the *velocity-delay map* and represents the response of the BLR gas to a instantaneous outburst of the continuum radiation. When integrated over all time delays, $\Psi(v,\tau_d)$ produces the line profiles and when integrated over all velocities, $\Psi(v,\tau_d)$ produces the $\Psi(\tau_d)$ or the *1D transfer function*, which is also called the *delay map*.
One of the goals of reverberation mapping campaigns is to construct velocity-delay maps for the observed objects, which provide a detailed picture of the structure and kinematics of the responding gas. However, this proves to be a difficult deconvolution problem if the data are noisy and not well sampled. Recovering delay map is also not straight forward. However, by cross-correlation analysis of continuum and integrated emission light curves, centroid of the delay map could be estimated.

3.2 Reverberation Mapping Results

3.2.1 Emission Line Lag Measurements

As of now, emission line lags have been determined for close to 100 AGNs. (e.g.; Peterson et al. (2004); Kaspi et al. (2000); Kaspi et al. (2005); Bentz et al. (2009); Bentz et al. (2010); Denney et al. (2010); Barth et al. (2015); Grier et al. (2012b); Grier et al. (2017); Du et al. (2014); Du et al. (2016a); Du et al. (2016b); Hu et al. (2015); Bentz & Katz (2015)). However, this sample is biased towards AGN with relatively strong emission lines. Although, most of the measurements that have been carried out so far are for low ionization line $H\beta$ in the optical region, same AGN can be studied using multiple UV and optical broad emission lines in their spectra. Measured time

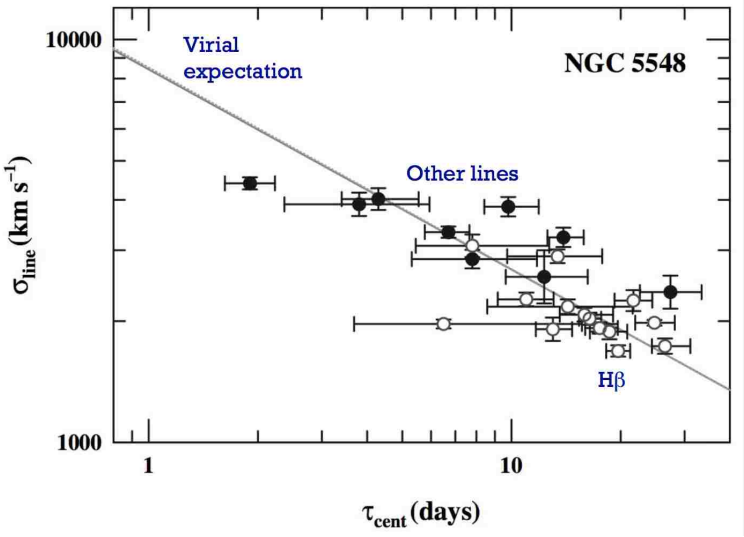

Figure 3.1: Evidence of BLR virialization:
Line width vs time delay plot for multiple emission lines at multiple epochs for NGC 5548. The solid line indicates the best fit line which coincides with slope -1/2 indicating a virial relationship. Open circles indicate H_β measurements and solid circles indicate all the other lines. Courtesy Peterson et al. (2004).

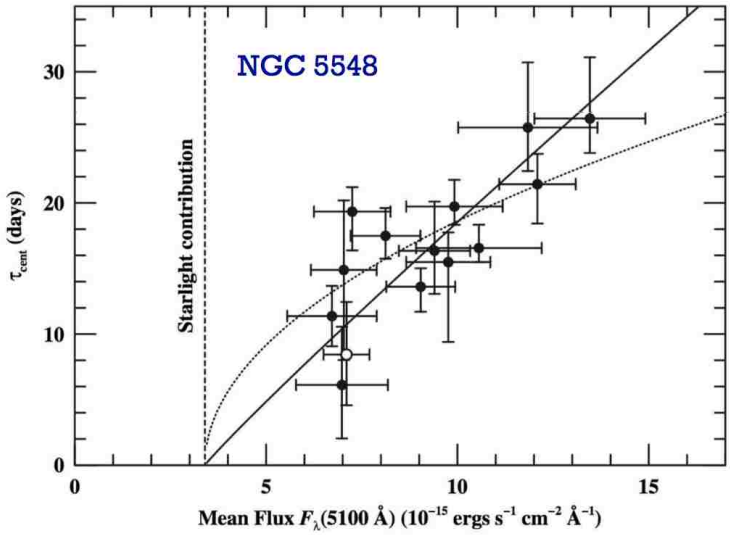

Figure 3.2: Evidence of BLR *breathing* effect:
Time delay for H_β vs optical continuum flux of NGC 5548 measured at 14 different experiments. The vertical line shows the constant stellar contribution to the measured continuum flux. The best-fit slope to this relationship is shown as a solid line $\tau \propto F^{0.9}$ and the dotted line shows the prediction $\tau \propto F^{0.5}$. Courtesy Peterson et al. (2002).

lags show that the highest ionization emission lines respond most rapidly to continuum variation indicating BLR must radially stratified. Moreover, the higher ionization lines also tend to have broadest widths indicating that BLR must be virialized. (See Figure 3.1)

BLR of few well studied AGN such as NGC 5548 have exhibited *breathing* effect (Peterson et al. (2002)); seemingly expanding and shrinking in time scales of ~ 1 year, corresponding to going from low-luminosity states to high-luminosity states and vice versa. This manifest as higher time lags for higher luminosities and lower time lags for lower luminosities. Figure 3.2 illustrates this effect. It's important to note that, this is not to say that BLR gas physically expanding or shrinking. Rather, the reservoir of BLR gas stays stationary (in timescales of years) while the conditions for optimal ionization are satisfied at different distances from continuum source. For high luminosity states, optimal conditions for a given emission line would be satisfied farther away than at lower luminosity state. The reservoir of gas present in the BLR is $\sim 1000 - 10000$ $M_\odot$ and only less than $\sim 1\%$ radiates lines efficiently at a given time (Baldwin et al. (2003)).

Because AGN spectra are similar over a wide range of luminosity, it is reasonable to infer that when individual emission line is considered, physical conditions under which they form in BLR are similar across AGN as well. This means that for a given emission line, U and n_e in equations 2.1 and 2.2 could be assumed to be unchanged across different AGN. This leads to the relation between BLR radius r and continuum luminosity L

$$r \propto L^{1/2} \tag{3.2}$$

Since the average BLR radius is simply the light crossing time $c\tau_d$ where, τ_d is the time lag of the emission line, we have

$$\tau_d \propto L^{1/2} \tag{3.3}$$

Figure 3.3 shows the that reverberation mapping data supports this relation.

Due to the ionization stratification of BLR, time lags for different emission lines for the same AGN are different. Therefore, it's important to remember that the R_{BLR} in $R_{BLR} - L$ relation is mean radius of the emission line considered.

3.2.2 Black Hole Mass Estimations

Virial theorem states that sum of twice the kinetic energy of a system and the potential energy is zero. All reverberation mapped AGN with variable emission line widths (ΔV) and corresponding time delays (τ_d) measured show consistency with the virial relationship. This suggests that the BLR is under the influence of the gravitational potential of the central SMBH of the AGN allowing us to find an expression for M_{BH} in terms of measured quantities.

$$M_{\rm BH} = f\left(\frac{\Delta V^2 c\tau_d}{G}\right) \tag{3.4}$$

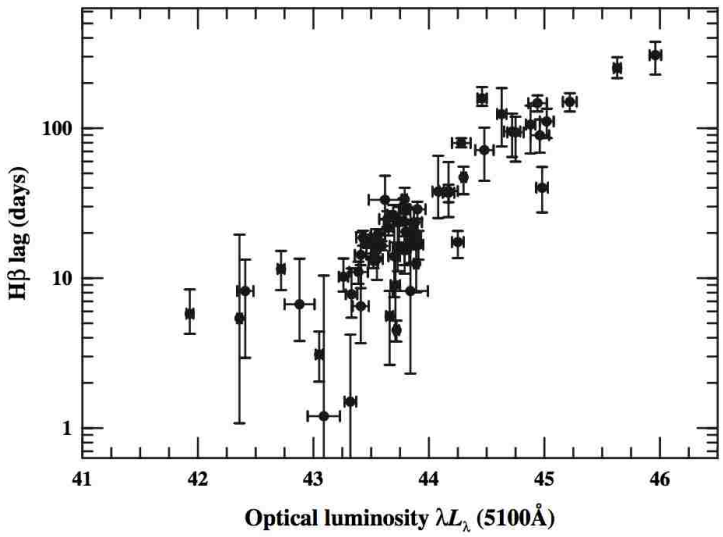

Figure 3.3: $R_{BLR} - L$ relation:
$H\beta$ lags vs optical continuum luminosity for ~ 30 reverberation-mapped AGN. Includes multiple measurements for some sources. For this data, $R_{BLR} \propto L^{0.6\pm0.1}$. Courtesy Peterson et al. (2004).

Here, the f is a dimensionless factor which accounts for unknown geometry, inclination and kinematics of the BLR. This method is a direct method of measuring black hole mass albeit a secondary method, since we have to rely on an independent method (i.e. the $M_{BH} - \sigma_*$ relation) to calibrate the black hole masses by calibrating $< f >$. By assuming that the $M_{BH} - \sigma_*$ relation of quiescent galaxies is the same as that of active galaxies, $< f >$ is determined to be $\sim 4 - 5$ (e.g.; Onken et al. (2004); Graham et al. (2011); Park et al. (2012); Grier et al. (2013)). For $H\beta$, masses measured this way are accurate to within ~ 3.

This method can be used to measure masses at high redshifts as well. However, such reverberation campaigns may take much longer (i.e. $\sim$ decades) due to luminous quasars in general have longer time lags and dues to cosmological time dilation exacerbating this effect even further.
Since reverberation mapping campaigns can be quite resource intensive, attempts have been made to determine single-epoch based black hole masses. By combining $R_{BLR} - L$ relation with virial theorem, single epoch black hole masses can be estimated (e.g., Kaspi et al. (2000)). For example using $H\beta$ (see equation 3 in Trakhtenbrot & Netzer (2012)),

$$\frac{M_{BH}(H\beta)}{10^8\ M_\odot} = 1.05 \left[\frac{\nu L_\nu(5100\ \text{Å})}{10^{46}\ \text{ergs s}^{-1}}\right]^{0.65} \left[\frac{FWHM(H\beta)}{10^3\ \text{km s}^{-1}}\right]^2 \tag{3.5}$$

Similar calculations can be carried out with other emission lines as well (e.g.; equation 12 in Trakhtenbrot & Netzer (2012)).
It is worth noting that since these are single epoch calculations, instead of RMS full width at half

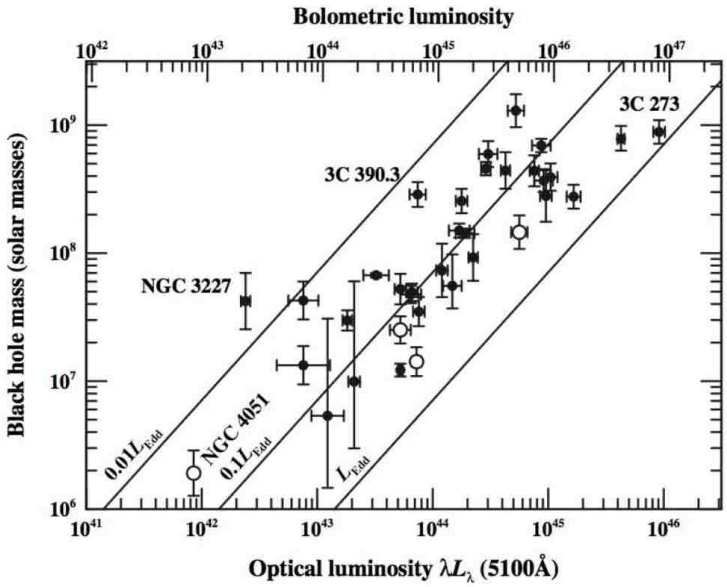

Figure 3.4: $M_{BH} - L$ relation:
Mass-Luminosity relation for 35 reverberation mapped AGN. The luminosity scale on the lower x-axis is $log\lambda L_\lambda$ in units of ergs s^1. The upper x-axis shows the bolometric luminosity assuming that $L_{bol} = 9\lambda L_\lambda(5100\text{Å})$. The diagonal lines show the Eddington limit L_{Edd}, $0.1L_{Edd}$, and $0.01L_{Edd}$. The open circles represent NLS1s. Courtesy Peterson et al. (2004).

maximum (FWHM) of the emission line is used. This includes both stationary and variable parts of the line. Therefore, accuracy of single epoch mass estimations are much lower.

Chapter 4

BLR Models

A successful model of BLR should be able to recreate time-dependent profiles and equivalent widths of multiple emission lines obtained from RM experiments. Many possible configurations have been proposed over the years as candidate models for BLR. Some examples include: radiation pressure driven outflowing clouds (e.g.; Mathews & Capriotti (1985)), bloated stars or clouds in gravitationally bound orbits (e.g.; Alexander & Netzer (1994); Alexander & Netzer (1997); Goad & Wanders (1996)), Keplarian disks (e.g.; Dumont & Collin-Souffrin (1990a); Dumont & Collin-Souffrin (1990b); Rokaki et al. (1992); Jackson et al. (1991); Corbin (1997); Gilbert et al. (1999); Storchi-Bergmann et al. (2003); Schimoia et al. (2012)), and accretion disk winds (e.g.; Shields (1977); Emmering et al. (1992); Murray et al. (1995); Bottorff et al. (1997)). Where and how does the BLR gas originate and whether the BLR gas is an extension of the accretion flow itself are some of the questions that need to be answered. Therefore, the exact nature of BLR remains elusive to date. Below we briefly discuss some of the proposed models, adapted from the review paper Peterson (2006).

4.1 Cloud Models

The earliest models devised for BLR were influenced by filament-like (or cloud-like) structures of supernova remnants, such as that of the Crab Nebula. The reason being, both BLR and supernova display supersonic bulk motions associated with large scale outflows.

For a detailed description of cloud models refer to Peterson (2006). Cloud models assume that the BLR is composed of a huge number N_c of identical line-emitting clouds with radius R_c. Then, the BLR covering factor (i.e., percentage of the sky concealed by BLR clouds, from the point of view of

the central source) is proportional to $N_c {R_c}^2$. By estimating the percentage of ionizing continuum photons absorbed by BLR clouds and reprocessed into emission line photons, the covering factor can be determined. It is estimated to be about $\sim 10\%$ by the equivalent widths of the emission lines. The total line luminosity provides an independent constraint. The total line luminosity is proportional to $N_c {R_c}^3$, which is the total volume of line-emitting material. Combining these two independent constraints, N_c and R_c could be independently calculated. For a typical Seyfert galaxy like NGC 5548, calculated values turn out to be $N_c \approx 10^7$ (Arav et al. (1998); Dietrich et al. (1999)) and $R_c \approx 10^{13}$ cm. Also, cloud column density of $N_H \approx 10^{23}$ cm^2 can be calculated by the particle density $n_e \approx 10^{10}$ cm^3 with the cloud size. By coincidence, this happens to be the same order of magnitude as the early measurements of the column densities of so called *warm absorbers* observed in the AGN X-ray spectra. Therefore, this absorption was attributed to BLR clouds obscuring the small X-ray continuum source. With above mentioned values for density, size, and number of the clouds, the mass for the BLR turns out to be ~ 1 M$_\odot$. Observations over time has revealed that this is a gross underestimation; since at any epoch only the responding gas is detected. The mass of the total reservoir of gas is estimated to be $\sim 10^3 - 10^4$ M$_\odot$ (Baldwin et al. (2003)).

Both ballistic outflow (as seen in supernova remnants) and radiation pressure driven outflow can give rise to logarithmic line profiles. Early on, outflow BLR models were favored due to the fact that the notion of virialized BLR seemed unlikely. Modeling of photoionization equilibrium was the only way to calculate BLR size before reverberation mapping became mainstream. Mass estimates derived by photoionization models were inconsistent with observed stellar dynamics in the nuclear region. This was because the size predicted by those models were too large by an order of magnitude. It turns out that the reasoning behind the number of emitting clouds is erroneous. It is logical to infer that the BLR clouds are optically thick since emission lines follow continuum variations. In that case, effective volume of a single cloud that which is responsible for line emission is proportional to the Strömgren depth R_S and is given by ${R_c}^2 R_S$. This implies that number of clouds and cloud size are no longer independently constrained. Another proposed scenario supporting a large number of clouds is that individual clouds emit thermally with widths ~ 10 km s^{-1}, and many of them collectively produce the velocity dispersion $\sim 10^4$ km s^{-1} explaining observed emission line widths. However, lack of grainy structure that would be present in line profiles due to its composite nature if this were the case even in high spectral resolution debunks this idea. This suggests that the BLR may be composed of a continuous flow gas. The BLR of NGC 4395, which contains one of the smallest SMBH, could only contain a few thousand clouds due to its small size far below than the

derived value (10^7). If it indeed contain only a small number of clouds (i.e. in the order thousands), this would manifest in line profiles as grainy structure. Since observations of NGC 4395 produce smooth line profiles, only possible scenario (in the absence of other sources of microturbulence) with cloud model of BLR involves supersonic flows. However, this model was refuted later on the basis that such clouds would be quickly destroyed by hydrodynamical instabilities (Mathews (1986); Krolik (1988)).

4.2 Bloated Stars Model

Another dismissed model of BLR is the bloated star model. Bloated stars were thought to be stars in the AGN nuclear region with extended envelopes due to their interaction with the intense radiation field. They were also thought to be produced by star-star collisions. While bloated star model holds up well in terms of cloud stability problem encountered in the previous model, it raises other questions (Arav et al. (1997). Their stellar surface gravity is too high to remove gas except for in case of giant stars, which are less abundant compared to their smaller counterparts. Also, the number of stars that would fit in the BLR turns out to be $\sim 10^5$, which is similar to the number of clouds problem encountered in the previous model.

4.3 Rotating disk Model

Accretion disks and Galactic binaries produce characteristic double-peaked line profiles. Only a small percentage of the broad line profiles feature double peaks (e.g., Eracleous & Halpern (1994); Eracleous & Halpern (2003); Strateva et al. (2003);). They could appear in RMS spectra or difference spectra. However, modeling such disks are not trivial. Although understanding the sources which produce double-peaked line profiles are important, rotating disk models by themselves do not explain all the characteristics of BLR. Also, whether the rest of the AGN which do not show doublepeaked emission lines in their broad line spectra contain disk structures that happen to be obscured, is ambiguous.

4.4 Disk-wind Models

Disk-winds are widely accepted as BLR models due to mounting evidence supporting this idea (Murray et al. (1995); Bottorff et al. (1997); Proga et al. (1999); Proga & Kallman (2004)). In addition to broad emission lines, quasar broad absorption lines (BAL) could also be understood

using this model (Arav et al. (1994); Proga et al. (1999);Proga et al. (2000)). In these models, the winds are driven either radiatively or hydromagnetically or by a combination of the two phenomena.

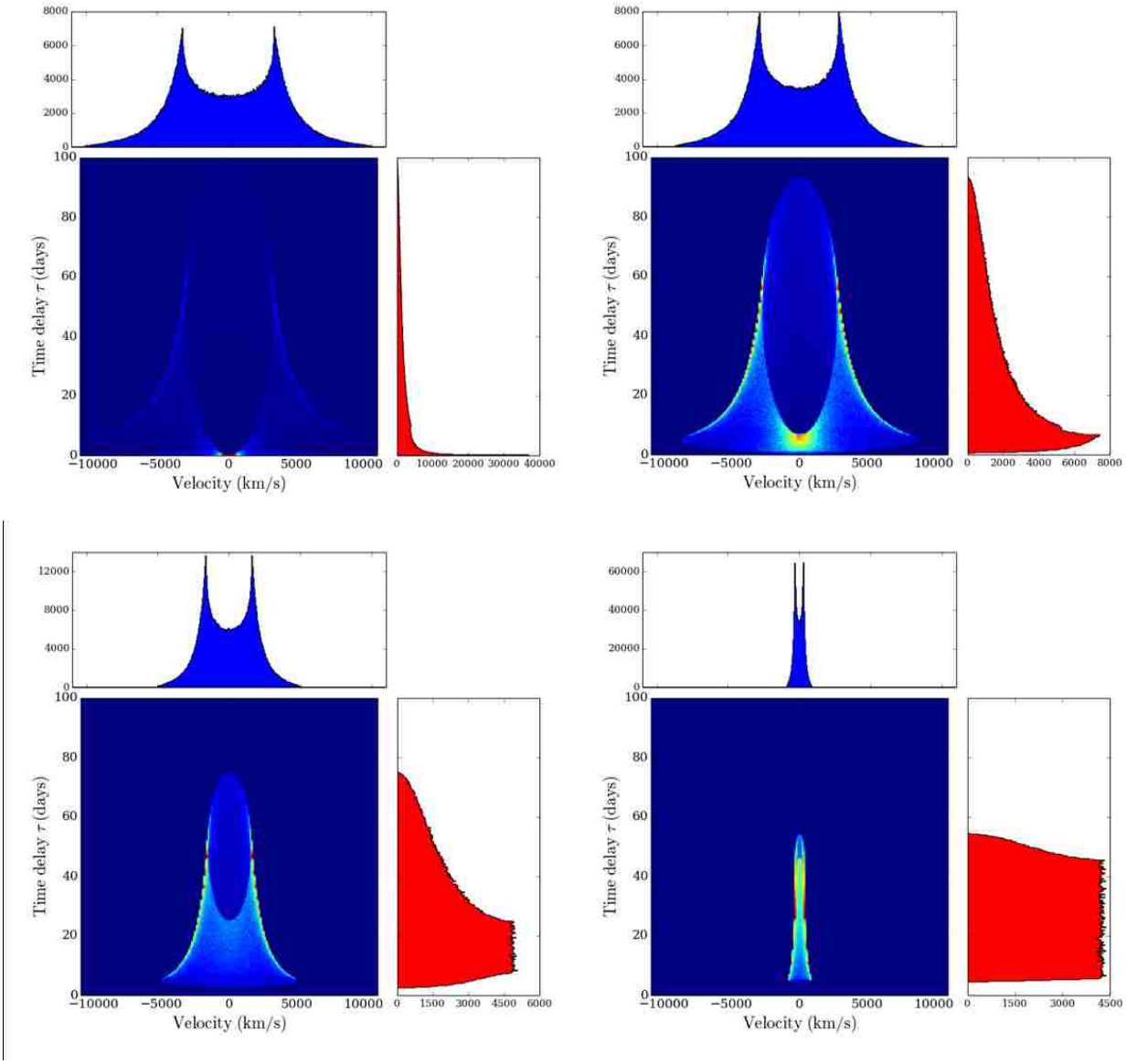

Figure 4.1: Echo images of a thin Keplerian disk BLR model viewed at different inclination angles reproduced from Welsh & Horne (1991).
The panels represent, top left: 90°, top right: 60°, bottom left: 30°, bottom right: 5°.
Each panel displays 2D echo image (middle), 1D echo image (right), and line profile (upper). 1D echo image and line profile are obtained by summing over the time delay bins and velocity bins of the 2D echo image respectively. The density variation in 2D echo image from highest to lowest is given by red, yellow, green, and, blue respectively.

Chapter 5

Constraining Parameters of a Disk-Wind Model

5.1 Why Disk-Wind Model?

As discussed in Chapter 4, various BLR models have been proposed as candidates over the years. Moreover, there have been attempts to model reverberation mapping datasets to place constrains on both BLR geometry (e.g.; Li et al. (2013)) and kinematics (e.g.; Pancoast et al. (2011); Brewer et al. (2011); Pancoast et al. (2014)). However, such phenomenological models do not take into account hydrodynamics and radiative transfer.

A very good reason to explore a disk-wind model of the BLR is that it is able to produce single-peaked line profiles which are much more abundant in observations than double-peaked line profiles. In the case of a simple Keplerian disk model of the BLR, symmetric redshifted and blueshifted emission along with symmetric time lags will give rise to double peaked emission line profiles if isotropic emission from the surface of the disk is assumed. The disk wind model (Murray et al. (1995)) solves this problem by invoking a wind which gives rise to anisotropic line emission. The emission is produced by the combined effect of shears in the disk and radiatively driven disk wind. These models produce single peaked line profiles without the need for unrealistically large BLR radii (e.g.; Chiang & Murray (1996); Murray & Chiang (1997); Waters et al. (2016)).

Chiang & Murray (1996) use a Keplerian disk with a radial photoionized wind as the BLR model and calculate the echo images and line profiles. In this Chapter we build up on that work with the aim of testing our ability to recover the parameters of a given model when compared with observational data.

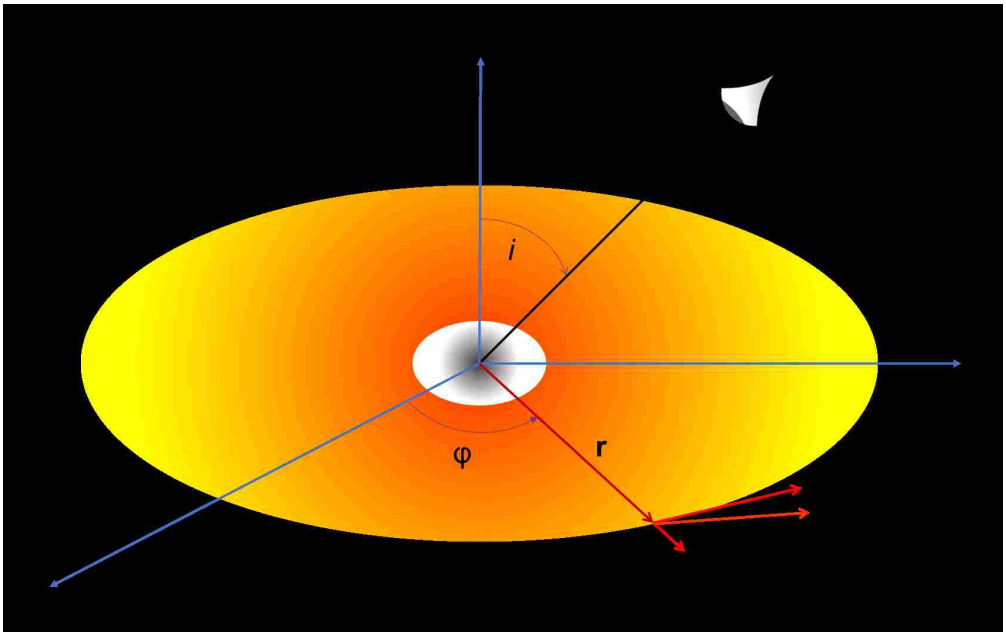

Figure 5.1: A schematic diagram showing the geometry of a disk-wind model of the broad-line region. The gas at a location (r, ϕ) will have two components to the velocity, v_r due to the radially outflowing wind, and, v_ϕ due to the rotational motion. The disk inclination with respect to the observer is indicated by angle i.

5.2 Model

We use a simple thin Keplarian disk model with a purely radial wind component (see Figure 5.1) as described in Chiang & Murray (1996). The velocity of the gas is composed of a radial component v_r due to the wind and an azimuthal component v_ϕ due to the rotational motion in the gravitational potential of the central black hole, and, is given by,

$$\mathbf{v} = v_r \hat{\mathbf{r}} + v_\phi \hat{\boldsymbol{\phi}}, \tag{5.1}$$

subjected to two constraints. The first constraint arises from the fact that observations (Korista et al. (1995)) suggest that the bulk radial velocity of the line emitting gas is small, while requiring large rotational velocities due to large line widths.

$$v_r << v_\phi \tag{5.2}$$

The second constraint arises from the fact that the observed line profiles are single peaked. This is due to the presence of large radial shear in the radial velocity of emitting gas which is comparable to that of rotational velocity (Murray & Chiang (1997)).

$$\frac{dv_r}{dr} \gtrsim \frac{dv_\phi}{dr} \tag{5.3}$$

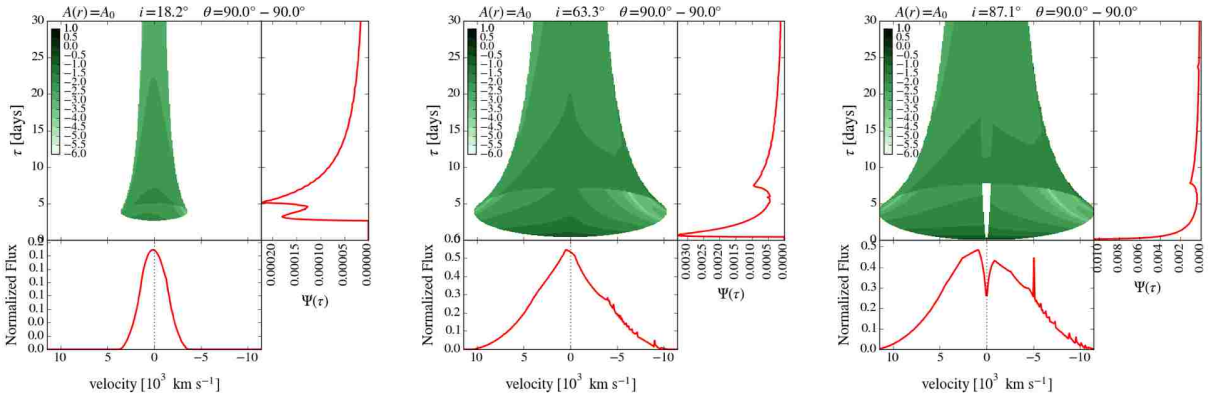

Figure 5.2: Echo images for $\eta = 0$ with three different inclination angles: $i = 18.19°, 63.26°$ and $87.13°$ (i.e. $\cos i = 0.95, 0.45$ and 0.05) respectively. Each panel displays 2D echo image (upper left), 1D echo image (upper right), and line profile (lower left) of Chiang & Murray (1996) disk wind model. 1D echo image and line profile are obtained by summing over the time delay bins and velocity bins of the 2D echo image respectively.

For an outside observer who sees the disk with an inclination angle i, the projected velocity along the line of sight is,

$$v_{proj} = \sin i(v_r \sin\phi + v_\phi \cos\phi), \tag{5.4}$$

Azimuthal component of the velocity is given by,

$$v_\phi = \sqrt{\frac{2GM}{r}}, \tag{5.5}$$

For a black-hole of mass $\simeq 10^8 M_\odot$, $v_r \sim 10^7$ cm s^{-1} in the vicinity of disk surface, and, $v_\phi \sim 10^8 - \sim 10^9$ cm s^{-1} throughout the broad line emitting region. Therefore, the projected velocity along the line of sight reduces to

$$v_{proj} \simeq \sqrt{\frac{GM}{r}} \sin i \cos\phi, \tag{5.6}$$

Responsivity of the BLR gas which is defined as $\partial j_\nu / \partial F_X$, where j_ν is the monochromatic emission coefficient (i.e. emissivity) and F_X is the continuum flux, is a measure of the amount of response from the BLR gas to contiuum radiation. Responsivity varies as r^η, where η is the responsivity parameter. In Chiang & Murray (1996), only $\eta = 0$ scenario is considered. In this work, we take different values of η in our calculations.

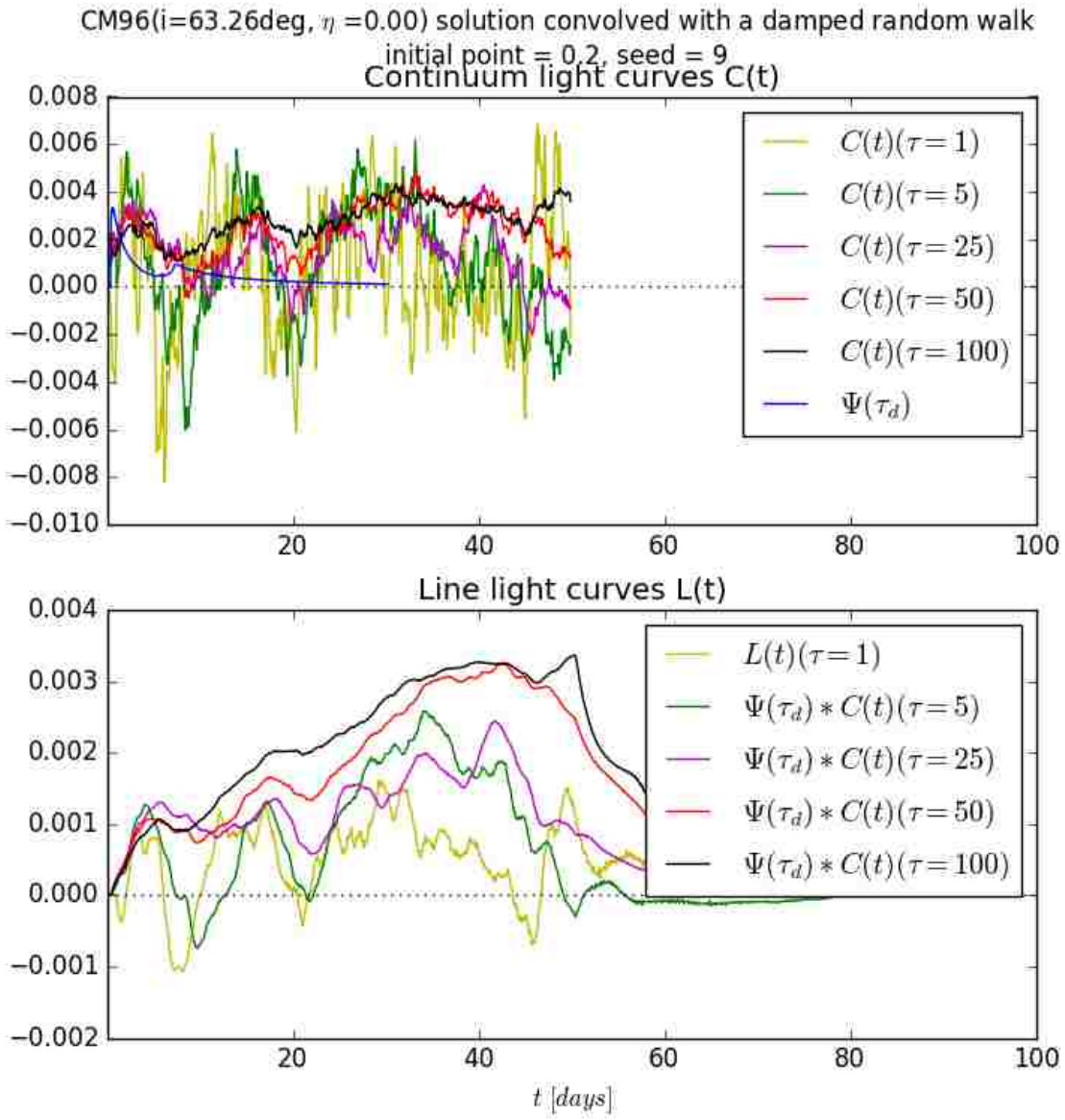

Figure 5.3: Upper panel: Simulated continuum light curves generated using different damping timescales τ. The blue line indicates the 1D echo function $\Psi(\tau_d)$ of a disk-wind BLR with an inclination angle $i = 63.26°$ (i.e. $\cos i = 0.45$) and responsivity parameter $\eta = 0$. Lower panel: Corresponding integrated line light curves obtained by convolving 1D echo function with continuum light curves.

5.3 Method

5.3.1 Bayesian Formalism

In order to constrain the parameters of the disk wind model of the BLR, we use Bayesian probability theory (Sivia & Skilling (2006)) to infer the model parameters θ, from a given set of reverberation mapped line light curve data D. From Bayes′ theorem,

$$p(\theta|D,I)p(D|I) = p(D|\theta,I)p(\theta|I) \tag{5.7}$$

$$Posterior \text{ x } Evidence = Likelihood \text{ x } Prior$$

where,

$p(\theta|I)$ – the prior probability distribution of the model parameters θ given any background information I, before the data D (i.e. the current evidence) is observed.

$p(D|\theta,I)$ – the *likelihood* or the probability of observing data D given the model with parameters θ and background information I.

$p(\theta|D,I)$ – the posterior probability distribution of model having the parameters θ, given the observed evidence D.

$p(D|I)$ – the *model evidence* or the *marginal likelihood*, which is simply the normalization constant of posterior probability distribution, which is the same for all possible parameter combinations.

The likelihood function is taken to be the product of Gaussian probabilities:

$$p(\theta|D,I) = \prod_i \frac{1}{\sigma\sqrt{2\pi}} e^{\left[-\frac{1}{2\sigma^2}(D_i - m_i(\theta)^2\right]}. \tag{5.8}$$

Here, our observation is the time series of total line flux D, the model is time series of predicted line light curves for a given BLR configuration $m(\theta)$ and the uncertainty of observation of each data point is σ.

In real reverberation mapping data, observations are composed of two data sets; time series of continuum fluxes and line fluxes. Since we are using simulated data exclusively and simulated *observed* line light curves and *model* line light curves were generated from the same continuum light curve, omitting continuum light curve from our data is justified.

5.3.2 Continuum Light Curves

We model the logarithm of continuum flux $X(t)$ as a *continuous autoregressive process* of order 1, CAR(1); which is described by the following stochastic differential equation.

$$dX(t) = -X(t)dt + \sigma\sqrt{\tau}\epsilon(t)dt + b\tau dt \tag{5.9}$$

where a, b & σ are parameters and $t = t_{obs}/\tau$ where τ is the *relaxation time* of the process or *damping time scale*. Here, $\epsilon(t)$ is a Gaussian noise process centered around 0 with unit variance. Also, mean value $\overline{X}(t) = b\tau$ and variance $Var(X(t)) = \tau\sigma^2/2$ (Kelly et al. (2009); Ivezić & MacLeod (2014)).

CAR(1) process is also called *damped random walk* (DRW) due to the damping term pushing $X(t)$ to its mean value. DRW has been found to describe the optical continuum variability of AGN well (e.g.;Kelly et al. (2009); Kozłowski et al. (2010); MacLeod et al. (2010)) and to be consistent with the time dependence of the *structure functon SF*

$$SF(\Delta t) = SF_\infty[1 - e^{(-\Delta t/\tau)}]^{1/2} \tag{5.10}$$

where $SF_\infty = \sigma\sqrt{\tau/2}$. For an AGN, SF is a measure of RMS magnitude difference as a function of time lag between magnitude measurements. The SF is related to autocorrelation function which makes a Fourier pair with power spectrum

$$PSD(f) = \frac{\tau^2 SF_\infty^2}{(1 + 2\pi f t)} \tag{5.11}$$

5.3.3 Line Light Curves

We take 2D echo images $\Psi(\nu, \tau_d)$ (see Figure 5.2) described in Chiang & Murray (1996) calculated using numerical methods (refer to Figure. 1 in the Appendix of Waters et al. (2016)) and convolve them with a simulated DRW continuum light curve $C(t)$ to obtain velocity-resolved line light curves $L(\nu, t)$.

$$L(\nu, t) = \int_0^\infty \Psi(\nu, \tau_d) C(t - \tau_d) d\tau_d \tag{5.12}$$

The integrated line light curves $L(t)$ (see Figure 5.3) are then obtained by summing over all velocity bins. The parameters varied were the inclination angle of the disc i, and the responsivity parameter of the gas η. These were varied independently and together giving rise to three separate cases.

Line light curves generated using echo images without normalizing their total flux first, will in general differ from each other in both flux and the shape. But, if the echo images were normalized in flux first, predicted line light curves will differ mainly in shape due to the differences in only the model parameter combinations. Since we have no information on the inclination angle in observational data, and flux differs greatly due to inclination angle, we only examine the latter scenario in

this work. Our *observation* is also generated in the same manner that the *models* are generated. Although it is possible to assign individual uncertainties to each data point in the observation, for simplicity we consider that the uncertainty of measurement is a constant for the whole series as could be the case if observations were made using the same instrument under the same observing conditions. The value of σ was determined to be consistent with uncertainty values in LAMP 2008 Hβ light curve data (Bentz et al. (2009)) which implied uncertainty values of less than 3% of line light curve fluxes. In this work, we assume a fixed value of about 5% of the mean of the *observation* for the value of σ, generate a Gaussian series of uncertainty values with standard deviation σ, and, add it to the *observation* in order to realistically simulate an observed data set. Therefore, each time this is done, a different realization of the same *observation* is generated. Only for the case of two-parameter variation, we included an analysis carried out with $\sigma = 20\%$ of the mean of the *observation* as well, in order to see how would a higher uncertainty in observation affect the inferred values.

Then, we compare the *observation* to the set of *models* using above described Bayesian inference framework and calculate the set of likelihood functions which is simply the posterior probability distribution. We use cubic interpolation between likelihood values to determine the maximally like parameter value more accurately. We repeat this process many times (1000 times for single parameter variation, and, 100 times for two parameter variation), plot a histogram of the maximally likely parameter values, and, pick the mean value of the distribution as our inferred parameter value. We determine the uncertainty of the inferred parameter by calculating the rms to the each side of the mean value. This uncertainty is a lower limit on the actual uncertainty since we have not taken into account systematic errors.

a) Inclination angle i (with $\eta = 0$):

A set of *observations* was generated with 10 i_{obs} values and each one was compared with a set of models generated using 150 i_{mod} values. There was no overlap between i_{obs} and i_{mod}. This was carried out with light curves generated using 3 different damping time scales. The histograms were constructed using cos i bins of 0.002.

b) Responsivity parameter η (for 3 different i values):

A set of *observations* was generated with 5 η_{obs} values and each one was compared with a set of models generated using 50 η_{mod} values. There was no overlap between η_{obs} and η_{mod}. The his-

tograms were binned in η pixels of 0.01.

c) Responsivity parameter η and inclination angle i:

Three cases were studied using three different combinations of grid resolutions and uncertainty in *observation*: A low resolution grid with low uncertainty in observation (i.e. $\sigma = 5\%$), a high resolution grid with low uncertainty in observation (i.e. $\sigma = 5\%$), and, a high resolution grid with high uncertainty in observation (i.e. $\sigma = 20\%$), The low resolution grid of models (51 x 48) was generated using 51 η_{mod} values and 48 i_{mod} values. The high resolution (3 times higher resolution in cos i_{mod} values) grid of models (51 x 143) was generated using 51 η_{mod} values and 143 i_{mod} values. In all cases, the model grids were compared to a grid of *observations* generated using 24 η_{obs} values and 3 i_{obs} values, and, were binned in pixels of $\Delta\eta$ x Δ cos i = 0.01 x 0.001. As in single parameter cases, there was no overlap between models and *observations*.

5.4 Results

a) Inclination angle i (with $\eta = 0$):

Table 5.1: Inferred value of cos i for $\eta = 0$ using simulated continua generated for different DRW damping time scales τ.

cos i_{obs}	for $\tau = 1$ days	$\tau = 5$ days	$\tau = 25$ days
0.050	$0.047^{+0.005}_{-0.001}$	$0.048^{+0.004}_{-0.005}$	$0.046^{+0.008}_{-0.006}$
0.150	$0.153^{+0.002}_{-0.006}$	$0.153^{+0.003}_{-0.007}$	$0.152^{+0.006}_{-0.014}$
0.250	$0.250^{+0.003}_{-0.003}$	$0.251^{+0.002}_{-0.004}$	$0.251^{+0.002}_{-0.005}$
0.350	$0.351^{+0.002}_{-0.004}$	$0.351^{+0.003}_{-0.004}$	$0.350^{+0.003}_{-0.004}$
0.450	$0.451^{+0.002}_{-0.004}$	$0.452^{+0.001}_{-0.006}$	$0.452^{+0.001}_{-0.008}$
0.550	$0.549^{+0.004}_{-0.003}$	$0.549^{+0.004}_{-0.003}$	$0.550^{+0.004}_{-0.003}$
0.650	$0.648^{+0.006}_{-0.001}$	$0.647^{+0.006}_{-0.000}$	$0.648^{+0.011}_{-0.002}$
0.750	$0.751^{+0.003}_{-0.004}$	$0.750^{+0.004}_{-0.003}$	$0.750^{+0.004}_{-0.003}$
0.850	$0.848^{+0.006}_{-0.001}$	$0.849^{+0.005}_{-0.002}$	$0.850^{+0.003}_{-0.003}$
0.950	$0.947^{+0.006}_{-0.000}$	$0.949^{+0.004}_{-0.003}$	$0.951^{+0.003}_{-0.004}$

In all cases inferred values of cos i were in good agreement with the angle value of the *observation*. Histograms corresponding to $\tau = 5$ days are presented in Figure 5.4. The inferred values for all cases are presented in Table 5.1.

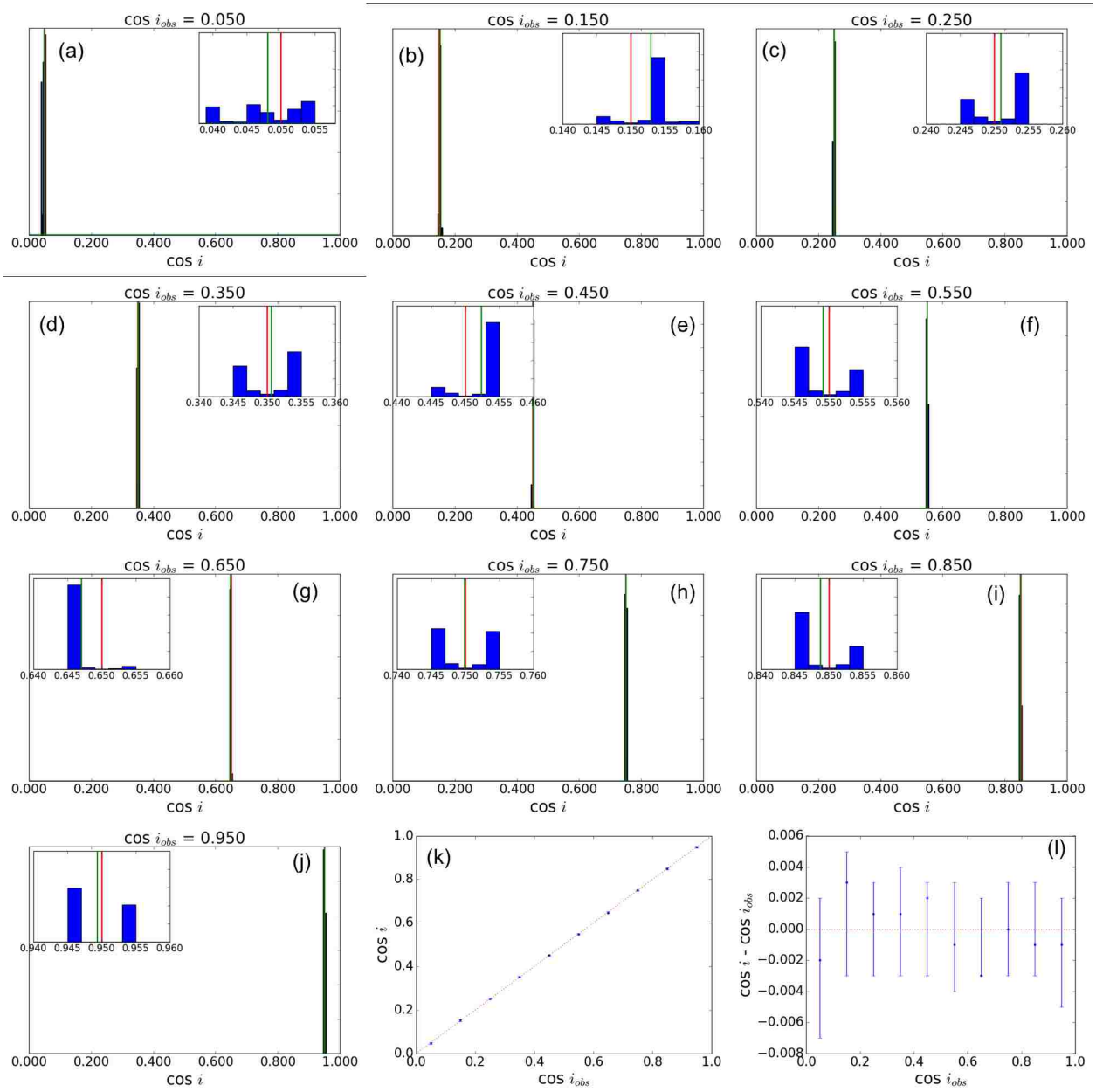

Figure 5.4: 1D histograms constructed using 1000 runs indicating inferred cosine value of inclination angle cos i for different *observation* values cos i_{obs} with responsivity parameter $\eta = 0$. Damping time scale of the continuum light curve used is 5 days.
Panels (a) through (j): Red and green vertical lines indicate cos i_{obs} and cos i (= mean of the distribution) respectively. Smaller panel within each panel is a zoom in of the region around cos i_{obs}. Panels (k) and (l) represent inferred cos i and residual cos i respectively, along with uncertainty values plotted against cos i_{obs}.

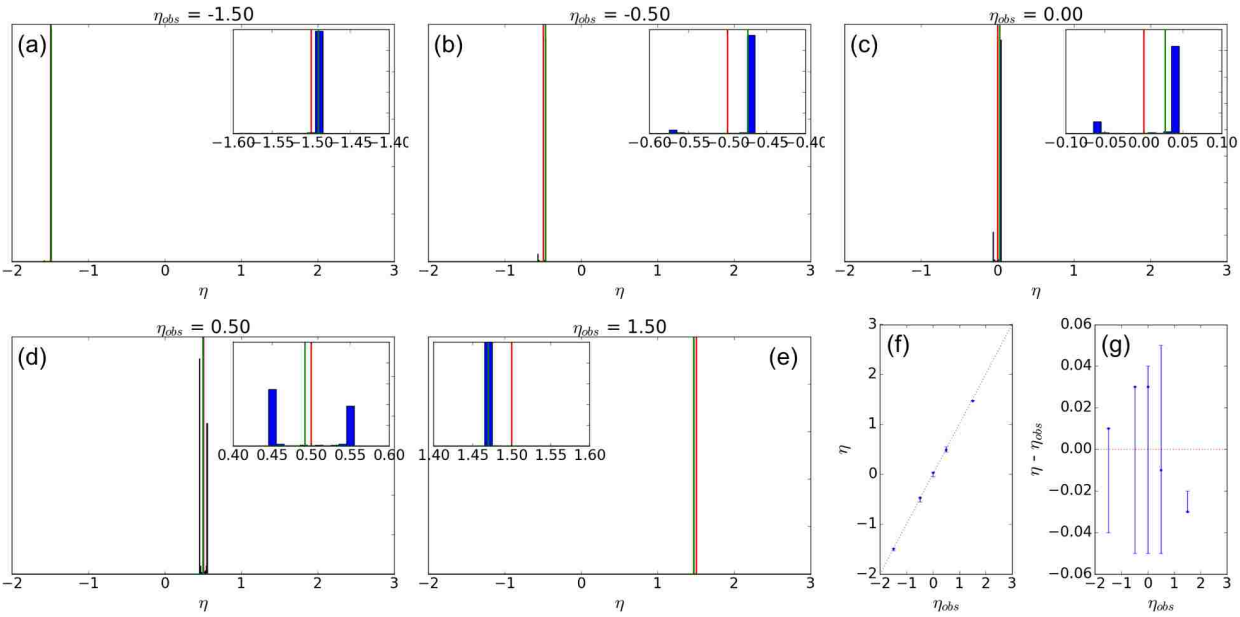

Figure 5.5: 1D histograms constructed using 1000 runs indicating inferred responsivity parameter η for different *observation* values η_{obs} when the disk inclination angle $i = 63.26°$. (i.e. cos i = 0.450)
Panels (a) through (e): Red and green vertical lines indicate η_{obs} and η (= mean of the distribution) respectively. Smaller panel within each panel is a zoom in of the region around η_{obs}. Panels (f) and (g) represent inferred η and residual η respectively, along with uncertainty values plotted against η_{obs}.

b) Responsivity parameter η (for 3 different i values):

All the inferred values of η agree quite well with the corresponding η value of the *observation* as evidenced by the Table 5.2. Histograms constructed for inclination angle $i = 63.26°$ (i.e. cos i = 0.450) are presented in Figure 5.5.

c) Responsivity parameter η and inclination angle i:

In all cases, the inferred values of cos i were of very high accuracy. For the most part, inferred values of η were of high accuracy as well. This deviated considerably for highest values of η_{obs} corresponding to cos i_{obs} = 0.050 in the low resolution grid with low σ (see Table 5.3). A sample of 2D histograms constructed for cos i_{obs} = 0.050 representing the 3 grids are presented in Figure 5.6. Overall, the high resolution grid with high σ (Table 5.4) fared better than the

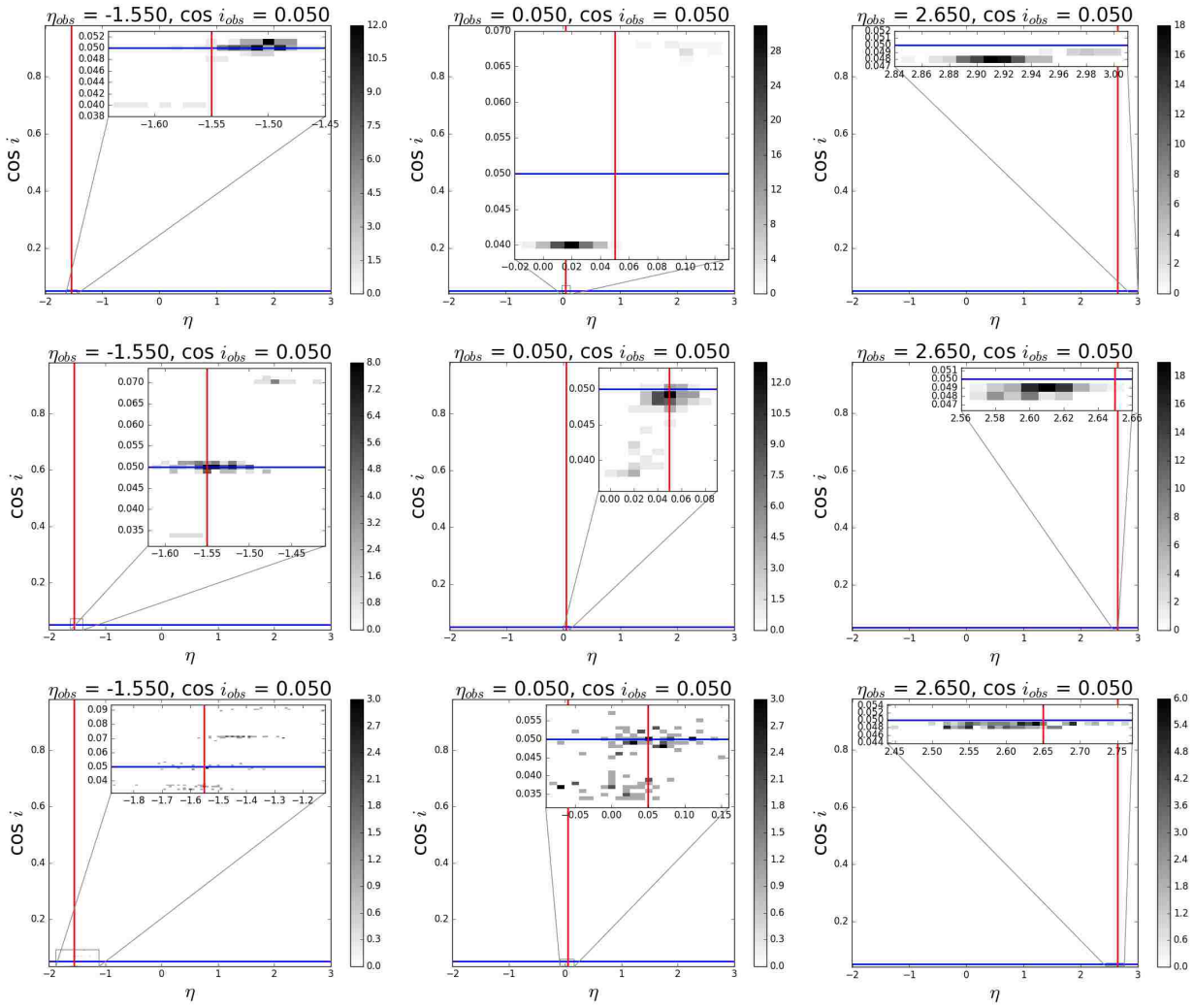

Figure 5.6: A sample of 2D histograms constructed using 100 runs in order to infer the responsivity parameter η and the cosine value of inclination angle cos i.
The 3 rows represents 3 different combinations of grid resolution and uncertainty in *observation*: The upper, middle, and, lower rows represent low grid resolution with $\sigma = 5\%$, high grid resolution with $\sigma = 5\%$, and, high grid resolution with $\sigma = 20\%$ respectively.
The 3 columns represent 3 different parameter parameter combinations in the *observation*: The left, middle, and, right columns represent (η_{obs}, i_{obs}) = (-1.55, 0.050), (0.05, 0.050), and, (2.65, 0.050) respectively.
In all panels the location of the observation in the histogram is indicated by the intersection of solid lines. Zoomed in portions of the histograms do not share the same magnification.

Table 5.2: Inferred value of η for three different inclination angles

η_{obs}	for $i = 18.19°$ ($\cos i_{obs} = 0.950$)	$i = 63.26°$ ($\cos i_{obs} = 0.450$)	$i = 87.13°$ ($\cos i_{obs} = 0.050$)
-1.50	$-1.49^{+0.00}_{-0.00}$	$-1.50^{+0.00}_{-0.05}$	$-1.49^{+0.00}_{-0.04}$
-0.50	$-0.47^{+0.00}_{-0.07}$	$-0.47^{+0.00}_{-0.08}$	$-0.48^{+0.01}_{-0.08}$
0.00	$0.04^{+0.00}_{-0.09}$	$0.03^{+0.01}_{-0.08}$	$0.02^{+0.02}_{-0.07}$
0.50	$0.50^{+0.05}_{-0.05}$	$0.49^{+0.06}_{-0.04}$	$0.50^{+0.05}_{-0.05}$
1.50	$1.47^{+0.00}_{-0.00}$	$1.47^{+0.01}_{-0.00}$	$1.50^{+0.06}_{-0.03}$

low resolution grid with low σ (Table 5.5) in terms of accuracy. Both high and low resolution grids with low σ displayed very small uncertainties in inferred values whereas the high resolution grid with the high σ displayed the highest amount of uncertainties. Overall, the inferred uncertainties tended to be extremely small, which could be a result of under estimating associated errors.

5.5 Discussion

We find that for largest inclination angles (i.e. $i > 80°$), the line profiles exhibit absorption like features. This could be due to shears not being large enough for the model parameters used. This does not carry significant implications since in real life scenarios, for such inclination angles, BLR is likely to be obscured by the torus.

When carrying out this analysis we have taken few measures to increase the efficiency of computations with minimal effects to the outcome. Here, we compute our 2D Echo images and transfer functions only up to a maximum delay of 30 days. As evident by the Figure 5.2, in all cases, total line flux is concentrated towards shorter time lags. This is specially true for larger inclination angles. Even for the smallest inclination angle, the loss of flux due to the cut off at $\tau = 30$ days is minimal. We compute the continuum light curves only up to 50 days and use the resulting full line light curve in our calculations.

5.6 Conclusions

We have tested the ability to constrain the parameters of a disk-wind model of the BLR using simulated data. We convolved echo images of the disk-wind model generated by varying inclination angle i and responsivity parameter η both individually and together, with a mock continuum generated by CAR(1) process to obtain mock line light curves. In each case, we used a similarly constructed line light curve as the *observation* and compared with the rest of the line light curves using Bayesian inference to recover the parameters of the *observation*. We further explored by using different *observations* covering full parameter range, and also tested the dependence of the results on the damping time scale by using light curves generated by three different damping time scales. Our results indicate that the results do not depend on damping time scale of the continuum light curves. In all tested cases we successfully constrained the inclination angle i. For $\cos i_{obs} = 0.950$ and 0.450, both low and high resolution grids constrained the parameter η equally well. A higher grid resolution improved the accuracy of the inferred values of parameter η corresponding to $\cos i_{obs} = 0.050$ by upto $\sim$ 13%.

Table 5.3: Inferred values of η and cos i by comparing the low resolution grid of models ((51) η_{mod} x (48) cos i_{mod}) to the grid of observations ((24) η_{obs} x (3) cos i_{obs}) Uncertainty of the observation = 5% of the mean of the observation.

η_{obs}	cos $i_{obs} = 0.950$ ($i_{obs} = 18.19°$)		cos $i_{obs} = 0.450$ ($i_{obs} = 63.26°$)		cos $i_{obs} = 0.050$ ($i_{obs} = 87.13°$)	
	η	cos i	η	cos i	η	cos i
-1.75	$-1.74^{+0.00}_{-0.01}$	$0.950^{+0.000}_{-0.000}$	$-1.79^{+0.01}_{-0.01}$	$0.451^{+0.000}_{-0.001}$	$-1.69^{+0.03}_{-0.02}$	$0.050^{+0.000}_{-0.001}$
-1.55	$-1.55^{+0.01}_{-0.00}$	$0.950^{+0.000}_{-0.000}$	$-1.58^{+0.01}_{-0.01}$	$0.451^{+0.000}_{-0.001}$	$-1.51^{+0.02}_{-0.04}$	$0.050^{+0.001}_{-0.007}$
-1.35	$-1.35^{+0.01}_{-0.00}$	$0.950^{+0.000}_{-0.000}$	$-1.38^{+0.01}_{-0.01}$	$0.451^{+0.002}_{-0.001}$	$-1.33^{+0.03}_{-0.04}$	$0.048^{+0.003}_{-0.008}$
-1.15	$-1.15^{+0.00}_{-0.01}$	$0.950^{+0.000}_{-0.000}$	$-1.17^{+0.01}_{-0.01}$	$0.451^{+0.000}_{-0.001}$	$-1.15^{+0.03}_{-0.04}$	$0.048^{+0.005}_{-0.008}$
-0.95	$-0.95^{+0.00}_{-0.00}$	$0.950^{+0.000}_{-0.000}$	$-0.97^{+0.01}_{-0.01}$	$0.451^{+0.000}_{-0.001}$	$-0.93^{+0.04}_{-0.40}$	$0.057^{+0.009}_{-0.015}$
-0.75	$-0.75^{+0.00}_{-0.01}$	$0.950^{+0.000}_{-0.000}$	$-0.77^{+0.01}_{-0.00}$	$0.451^{+0.000}_{-0.001}$	$-0.70^{+0.02}_{-0.03}$	$0.069^{+0.002}_{-0.016}$
-0.55	$-0.55^{+0.00}_{-0.01}$	$0.950^{+0.000}_{-0.000}$	$-0.57^{+0.01}_{-0.00}$	$0.451^{+0.000}_{-0.001}$	$-0.49^{+0.02}_{-0.02}$	$0.071^{+0.001}_{-0.005}$
-0.35	$-0.35^{+0.00}_{-0.01}$	$0.950^{+0.000}_{-0.000}$	$-0.36^{+0.00}_{-0.01}$	$0.451^{+0.000}_{-0.001}$	$-0.30^{+0.02}_{-0.04}$	$0.069^{+0.003}_{-0.029}$
-0.15	$-0.15^{+0.00}_{-0.01}$	$0.950^{+0.000}_{-0.000}$	$-0.16^{+0.00}_{-0.01}$	$0.451^{+0.001}_{-0.001}$	$-0.12^{+0.03}_{-0.05}$	$0.061^{+0.009}_{-0.021}$
0.05	$0.05^{+0.00}_{-0.00}$	$0.950^{+0.000}_{-0.000}$	$0.04^{+0.01}_{-0.00}$	$0.451^{+0.001}_{-0.001}$	$0.03^{+0.04}_{-0.02}$	$0.043^{+0.024}_{-0.003}$
0.25	$0.25^{+0.00}_{-0.01}$	$0.950^{+0.000}_{-0.000}$	$0.24^{+0.01}_{-0.00}$	$0.451^{+0.001}_{-0.001}$	$0.21^{+0.01}_{-0.01}$	$0.040^{+0.000}_{-0.000}$
0.45	$0.45^{+0.00}_{-0.01}$	$0.950^{+0.000}_{-0.001}$	$0.45^{+0.00}_{-0.01}$	$0.450^{+0.002}_{-0.001}$	$0.40^{+0.01}_{-0.01}$	$0.040^{+0.000}_{-0.000}$
0.65	$0.65^{+0.00}_{-0.00}$	$0.950^{+0.000}_{-0.001}$	$0.65^{+0.00}_{-0.01}$	$0.450^{+0.002}_{-0.001}$	$0.59^{+0.04}_{-0.01}$	$0.040^{+0.010}_{-0.000}$
0.85	$0.85^{+0.00}_{-0.00}$	$0.950^{+0.000}_{-0.000}$	$0.85^{+0.00}_{-0.01}$	$0.450^{+0.002}_{-0.001}$	$0.87^{+0.03}_{-0.08}$	$0.048^{+0.001}_{-0.007}$
1.05	$1.05^{+0.00}_{-0.00}$	$0.950^{+0.000}_{-0.001}$	$1.05^{+0.00}_{-0.01}$	$0.450^{+0.001}_{-0.001}$	$1.12^{+0.02}_{-0.02}$	$0.049^{+0.001}_{-0.000}$
1.25	$1.25^{+0.00}_{-0.00}$	$0.950^{+0.000}_{-0.000}$	$1.25^{+0.00}_{-0.01}$	$0.450^{+0.001}_{-0.001}$	$1.35^{+0.02}_{-0.02}$	$0.049^{+0.001}_{-0.000}$
1.45	$1.45^{+0.00}_{-0.00}$	$0.950^{+0.000}_{-0.001}$	$1.45^{+0.00}_{-0.00}$	$0.450^{+0.000}_{-0.001}$	$1.57^{+0.02}_{-0.01}$	$0.049^{+0.001}_{-0.000}$
1.65	$1.65^{+0.00}_{-0.00}$	$0.950^{+0.000}_{-0.000}$	$1.65^{+0.00}_{-0.01}$	$0.450^{+0.001}_{-0.001}$	$1.81^{+0.02}_{-0.02}$	$0.049^{+0.001}_{-0.000}$
1.85	$1.85^{+0.00}_{-0.00}$	$0.950^{+0.000}_{-0.001}$	$1.85^{+0.00}_{-0.00}$	$0.450^{+0.001}_{-0.000}$	$2.06^{+0.02}_{-0.02}$	$0.049^{+0.000}_{-0.000}$
2.05	$2.05^{+0.00}_{-0.00}$	$0.950^{+0.000}_{-0.001}$	$2.05^{+0.00}_{-0.00}$	$0.450^{+0.001}_{-0.000}$	$2.32^{+0.02}_{-0.02}$	$0.049^{+0.000}_{-0.000}$
2.25	$2.25^{+0.00}_{-0.00}$	$0.950^{+0.000}_{-0.000}$	$2.25^{+0.00}_{-0.00}$	$0.450^{+0.001}_{-0.000}$	$2.56^{+0.02}_{-0.02}$	$0.049^{+0.000}_{-0.001}$
2.45	$2.45^{+0.00}_{-0.00}$	$0.950^{+0.000}_{-0.000}$	$2.45^{+0.00}_{-0.00}$	$0.450^{+0.001}_{-0.000}$	$2.76^{+0.04}_{-0.02}$	$0.049^{+0.001}_{-0.000}$
2.65	$2.65^{+0.00}_{-0.00}$	$0.950^{+0.000}_{-0.001}$	$2.65^{+0.00}_{-0.00}$	$0.450^{+0.001}_{-0.000}$	$2.92^{+0.04}_{-0.02}$	$0.048^{+0.001}_{-0.000}$
2.85	$2.85^{+0.00}_{-0.00}$	$0.950^{+0.000}_{-0.001}$	$2.85^{+0.00}_{-0.00}$	$0.450^{+0.001}_{-0.000}$	$3.00^{+0.00}_{-0.00}$	$0.048^{+0.000}_{-0.000}$

Table 5.4: Inferred values of η and cos i by comparing the high resolution grid of models ((51) η_{mod} x (143) cos i_{mod}) to the grid of observations ((24) η_{obs} x (3) cos i_{obs}) Uncertainty of the observation = 5% of the mean of the observation.

η_{obs}	cos $i_{obs} = 0.950$ ($i_{obs} = 18.19°$)		cos $i_{obs} = 0.450$ ($i_{obs} = 63.26°$)		cos $i_{obs} = 0.050$ ($i_{obs} = 87.13°$)	
	η	cos i	η	cos i	η	cos i
-1.75	$-1.77^{+0.00}_{-0.01}$	$0.949^{+0.000}_{-0.000}$	$-1.78^{+0.01}_{-0.01}$	$0.451^{+0.000}_{-0.000}$	$-1.72^{+0.06}_{-0.04}$	$0.056^{+0.014}_{-0.006}$
-1.55	$-1.57^{+0.01}_{-0.00}$	$0.949^{+0.000}_{-0.000}$	$-1.57^{+0.01}_{-0.01}$	$0.451^{+0.000}_{-0.000}$	$-1.54^{+0.04}_{-0.03}$	$0.052^{+0.019}_{-0.004}$
-1.35	$-1.37^{+0.01}_{-0.00}$	$0.949^{+0.000}_{-0.000}$	$-1.37^{+0.01}_{-0.01}$	$0.451^{+0.000}_{-0.000}$	$-1.35^{+0.03}_{-0.03}$	$0.050^{+0.005}_{-0.006}$
-1.15	$-1.16^{+0.00}_{-0.01}$	$0.949^{+0.000}_{-0.000}$	$-1.17^{+0.01}_{-0.01}$	$0.451^{+0.000}_{-0.000}$	$-1.14^{+0.02}_{-0.02}$	$0.050^{+0.002}_{-0.006}$
-0.95	$-0.96^{+0.01}_{-0.00}$	$0.949^{+0.000}_{-0.000}$	$-0.96^{+0.00}_{-0.01}$	$0.451^{+0.000}_{-0.000}$	$-0.95^{+0.02}_{-0.03}$	$0.048^{+0.003}_{-0.014}$
-0.75	$-0.76^{+0.01}_{-0.00}$	$0.949^{+0.000}_{-0.000}$	$-0.76^{+0.00}_{-0.01}$	$0.451^{+0.000}_{-0.000}$	$-0.75^{+0.02}_{-0.03}$	$0.047^{+0.003}_{-0.012}$
-0.55	$-0.55^{+0.00}_{-0.01}$	$0.949^{+0.000}_{-0.000}$	$-0.56^{+0.01}_{-0.00}$	$0.451^{+0.001}_{-0.000}$	$-0.45^{+0.02}_{-0.02}$	$0.047^{+0.004}_{-0.011}$
-0.35	$-0.35^{+0.00}_{-0.01}$	$0.949^{+0.000}_{-0.000}$	$-0.36^{+0.01}_{-0.00}$	$0.451^{+0.000}_{-0.001}$	$-0.35^{+0.01}_{-0.02}$	$0.048^{+0.002}_{-0.012}$
-0.15	$-0.15^{+0.00}_{-0.01}$	$0.949^{+0.000}_{-0.000}$	$-0.15^{+0.00}_{-0.01}$	$0.451^{+0.000}_{-0.000}$	$-0.15^{+0.03}_{-0.05}$	$0.048^{+0.002}_{-0.010}$
0.05	$0.05^{+0.00}_{-0.00}$	$0.949^{+0.000}_{-0.000}$	$0.05^{+0.00}_{-0.01}$	$0.450^{+0.000}_{-0.000}$	$0.04^{+0.01}_{-0.02}$	$0.047^{+0.002}_{-0.007}$
0.25	$0.25^{+0.00}_{-0.00}$	$0.949^{+0.000}_{-0.000}$	$0.25^{+0.00}_{-0.01}$	$0.450^{+0.000}_{-0.000}$	$0.25^{+0.01}_{-0.01}$	$0.048^{+0.001}_{-0.002}$
0.45	$0.45^{+0.00}_{-0.00}$	$0.949^{+0.000}_{-0.000}$	$0.45^{+0.00}_{-0.01}$	$0.450^{+0.000}_{-0.000}$	$0.40^{+0.01}_{-0.01}$	$0.048^{+0.001}_{-0.001}$
0.65	$0.65^{+0.00}_{-0.00}$	$0.949^{+0.000}_{-0.000}$	$0.65^{+0.00}_{-0.00}$	$0.450^{+0.000}_{-0.000}$	$0.66^{+0.00}_{-0.01}$	$0.049^{+0.001}_{-0.001}$
0.85	$0.85^{+0.00}_{-0.00}$	$0.949^{+0.000}_{-0.000}$	$0.85^{+0.00}_{-0.00}$	$0.450^{+0.000}_{-0.000}$	$0.86^{+0.01}_{-0.01}$	$0.049^{+0.000}_{-0.001}$
1.05	$1.05^{+0.00}_{-0.00}$	$0.949^{+0.000}_{-0.000}$	$1.05^{+0.00}_{-0.00}$	$0.450^{+0.000}_{-0.000}$	$1.07^{+0.01}_{-0.01}$	$0.049^{+0.000}_{-0.000}$
1.25	$1.25^{+0.00}_{-0.00}$	$0.949^{+0.000}_{-0.000}$	$1.25^{+0.00}_{-0.01}$	$0.450^{+0.001}_{-0.001}$	$1.26^{+0.01}_{-0.01}$	$0.049^{+0.000}_{-0.000}$
1.45	$1.45^{+0.00}_{-0.00}$	$0.949^{+0.000}_{-0.000}$	$1.45^{+0.00}_{-0.00}$	$0.450^{+0.000}_{-0.000}$	$1.46^{+0.01}_{-0.01}$	$0.049^{+0.000}_{-0.000}$
1.65	$1.65^{+0.00}_{-0.00}$	$0.949^{+0.000}_{-0.000}$	$1.65^{+0.00}_{-0.00}$	$0.450^{+0.000}_{-0.000}$	$1.65^{+0.01}_{-0.01}$	$0.049^{+0.000}_{-0.000}$
1.85	$1.85^{+0.00}_{-0.00}$	$0.949^{+0.000}_{-0.000}$	$1.85^{+0.00}_{-0.00}$	$0.450^{+0.000}_{-0.000}$	$1.84^{+0.01}_{-0.01}$	$0.049^{+0.000}_{-0.000}$
2.05	$2.05^{+0.00}_{-0.00}$	$0.949^{+0.000}_{-0.000}$	$2.05^{+0.00}_{-0.00}$	$0.449^{+0.000}_{-0.000}$	$2.03^{+0.01}_{-0.01}$	$0.049^{+0.000}_{-0.000}$
2.25	$2.25^{+0.00}_{-0.00}$	$0.949^{+0.000}_{-0.000}$	$2.25^{+0.00}_{-0.00}$	$0.449^{+0.000}_{-0.000}$	$2.23^{+0.01}_{-0.02}$	$0.049^{+0.000}_{-0.00}$
2.45	$2.45^{+0.00}_{-0.00}$	$0.949^{+0.000}_{-0.000}$	$2.45^{+0.00}_{-0.00}$	$0.449^{+0.000}_{-0.000}$	$2.42^{+0.01}_{-0.02}$	$0.049^{+0.000}_{-0.000}$
2.65	$2.65^{+0.00}_{-0.00}$	$0.949^{+0.000}_{-0.000}$	$2.65^{+0.00}_{-0.00}$	$0.449^{+0.000}_{-0.000}$	$2.60^{+0.02}_{-0.02}$	$0.049^{+0.000}_{-0.000}$
2.85	$2.85^{+0.00}_{-0.00}$	$0.949^{+0.000}_{-0.000}$	$2.85^{+0.00}_{-0.00}$	$0.449^{+0.000}_{-0.000}$	$2.79^{+0.02}_{-0.02}$	$0.049^{+0.000}_{-0.000}$

Table 5.5: Inferred values of η and cos i by comparing the high resolution grid of models ((51) η_{mod} x (143) cos i_{mod}) to the grid of observations ((24) η_{obs} x (3) cos i_{obs}) Uncertainty of the observation = 20% of the mean of the observation.

η_{obs}	cos $i_{obs} = 0.950$ ($i_{obs} = 18.19°$)		cos $i_{obs} = 0.450$ ($i_{obs} = 63.26°$)		cos $i_{obs} = 0.050$ ($i_{obs} = 87.13°$)	
	η	cos i	η	cos i	η	cos i
-1.75	$-1.78^{+0.01}_{-0.01}$	$0.949^{+0.000}_{-0.000}$	$-1.78^{+0.04}_{-0.03}$	$0.451^{+0.001}_{-0.001}$	$-1.72^{+0.15}_{-0.12}$	$0.056^{+0.021}_{-0.015}$
-1.55	$-1.57^{+0.01}_{-0.01}$	$0.949^{+0.000}_{-0.000}$	$-1.57^{+0.03}_{-0.03}$	$0.451^{+0.001}_{-0.001}$	$-1.50^{+0.12}_{-0.12}$	$0.055^{+0.021}_{-0.015}$
-1.35	$-1.36^{+0.01}_{-0.01}$	$0.949^{+0.000}_{-0.000}$	$-1.37^{+0.02}_{-0.02}$	$0.451^{+0.001}_{-0.002}$	$-1.32^{+0.10}_{-0.12}$	$0.053^{+0.025}_{-0.012}$
-1.15	$-1.16^{+0.00}_{-0.01}$	$0.949^{+0.000}_{-0.000}$	$-1.17^{+0.02}_{-0.02}$	$0.451^{+0.001}_{-0.001}$	$-1.13^{+0.09}_{-0.10}$	$0.050^{+0.020}_{-0.011}$
-0.95	$-0.96^{+0.01}_{-0.01}$	$0.949^{+0.000}_{-0.000}$	$-0.96^{+0.02}_{-0.02}$	$0.451^{+0.001}_{-0.002}$	$-0.93^{+0.09}_{-0.09}$	$0.051^{+0.023}_{-0.013}$
-0.75	$-0.76^{+0.01}_{-0.01}$	$0.949^{+0.000}_{-0.000}$	$-0.76^{+0.02}_{-0.01}$	$0.451^{+0.001}_{-0.002}$	$-0.75^{+0.08}_{-0.07}$	$0.052^{+0.022}_{-0.012}$
-0.55	$-0.55^{+0.01}_{-0.01}$	$0.949^{+0.000}_{-0.000}$	$-0.56^{+0.02}_{-0.01}$	$0.451^{+0.002}_{-0.002}$	$-0.55^{+0.08}_{-0.07}$	$0.052^{+0.021}_{-0.012}$
-0.35	$-0.35^{+0.01}_{-0.01}$	$0.949^{+0.000}_{-0.000}$	$-0.36^{+0.01}_{-0.01}$	$0.450^{+0.002}_{-0.002}$	$-0.34^{+0.05}_{-0.06}$	$0.049^{+0.021}_{-0.011}$
-0.15	$-0.15^{+0.01}_{-0.01}$	$0.949^{+0.000}_{-0.000}$	$-0.15^{+0.01}_{-0.01}$	$0.451^{+0.002}_{-0.002}$	$-0.15^{+0.05}_{-0.05}$	$0.047^{+0.012}_{-0.011}$
0.05	$0.05^{+0.00}_{-0.01}$	$0.949^{+0.000}_{-0.000}$	$0.05^{+0.01}_{-0.01}$	$0.450^{+0.001}_{-0.001}$	$0.03^{+0.05}_{-0.05}$	$0.045^{+0.005}_{-0.008}$
0.25	$0.25^{+0.01}_{-0.00}$	$0.949^{+0.000}_{-0.000}$	$0.25^{+0.01}_{-0.01}$	$0.450^{+0.001}_{-0.002}$	$0.25^{+0.06}_{-0.06}$	$0.047^{+0.006}_{-0.008}$
0.45	$0.45^{+0.01}_{-0.00}$	$0.949^{+0.000}_{-0.000}$	$0.45^{+0.01}_{-0.01}$	$0.450^{+0.002}_{-0.002}$	$0.45^{+0.51}_{-0.05}$	$0.048^{+0.003}_{-0.005}$
0.65	$0.65^{+0.01}_{-0.00}$	$0.949^{+0.000}_{-0.000}$	$0.65^{+0.00}_{-0.01}$	$0.450^{+0.001}_{-0.001}$	$0.66^{+0.05}_{-0.05}$	$0.049^{+0.002}_{-0.002}$
0.85	$0.85^{+0.01}_{-0.00}$	$0.949^{+0.000}_{-0.000}$	$0.85^{+0.00}_{-0.01}$	$0.450^{+0.004}_{-0.003}$	$0.86^{+0.05}_{-0.05}$	$0.049^{+0.002}_{-0.002}$
1.05	$1.05^{+0.01}_{-0.00}$	$0.949^{+0.000}_{-0.000}$	$1.05^{+0.01}_{-0.01}$	$0.450^{+0.004}_{-0.004}$	$1.07^{+0.05}_{-0.05}$	$0.049^{+0.002}_{-0.001}$
1.25	$1.25^{+0.01}_{-0.00}$	$0.949^{+0.000}_{-0.000}$	$1.25^{+0.01}_{-0.02}$	$0.451^{+0.006}_{-0.004}$	$1.27^{+0.04}_{-0.04}$	$0.049^{+0.001}_{-0.001}$
1.45	$1.45^{+0.01}_{-0.00}$	$0.949^{+0.000}_{-0.000}$	$1.45^{+0.03}_{-0.01}$	$0.449^{+0.005}_{-0.008}$	$1.46^{+0.05}_{-0.05}$	$0.049^{+0.001}_{-0.001}$
1.65	$1.65^{+0.01}_{-0.00}$	$0.949^{+0.000}_{-0.000}$	$1.65^{+0.00}_{-0.02}$	$0.450^{+0.003}_{-0.003}$	$1.65^{+0.05}_{-0.04}$	$0.049^{+0.001}_{-0.001}$
1.85	$1.85^{+0.01}_{-0.00}$	$0.949^{+0.000}_{-0.001}$	$1.85^{+0.03}_{-0.00}$	$0.449^{+0.002}_{-0.005}$	$1.84^{+0.04}_{-0.04}$	$0.049^{+0.001}_{-0.001}$
2.05	$2.05^{+0.01}_{-0.00}$	$0.949^{+0.000}_{-0.001}$	$2.05^{+0.03}_{-0.00}$	$0.449^{+0.002}_{-0.004}$	$2.03^{+0.05}_{-0.05}$	$0.049^{+0.001}_{-0.000}$
2.25	$2.25^{+0.01}_{-0.00}$	$0.949^{+0.000}_{-0.001}$	$2.25^{+0.00}_{-0.01}$	$0.450^{+0.002}_{-0.002}$	$2.23^{+0.05}_{-0.05}$	$0.049^{+0.000}_{-0.000}$
2.45	$2.45^{+0.01}_{-0.00}$	$0.949^{+0.000}_{-0.001}$	$2.45^{+0.00}_{-0.01}$	$0.450^{+0.001}_{-0.000}$	$2.41^{+0.06}_{-0.04}$	$0.049^{+0.000}_{-0.000}$
2.65	$2.65^{+0.01}_{-0.00}$	$0.949^{+0.001}_{-0.001}$	$2.65^{+0.00}_{-0.01}$	$0.450^{+0.001}_{-0.000}$	$2.60^{+0.06}_{-0.06}$	$0.049^{+0.000}_{-0.000}$
2.85	$2.85^{+0.01}_{-0.00}$	$0.949^{+0.001}_{-0.001}$	$2.85^{+0.00}_{-0.01}$	$0.450^{+0.000}_{-0.000}$	$2.79^{+0.06}_{-0.06}$	$0.048^{+0.000}_{-0.000}$

Chapter 6

Constraining AGN Continuua

When constraining the parameters of a disk-wind model of the broad-line region, so far, we have employed only the simulated continuum light curves produced using a stochastic process called damped random walk. To assess the applicability of this model to real AGN broad line regions, we must feed in real AGN continuum light curves obtained by reverberation mapping campaigns.

Reverberation mapping datasets are composed of two time-series: AGN continuum light curves and broad emission line light curves. Usually, real light curves are not sampled frequently enough to resolve time scales less than a day. Due to a variety of factors such as instrumentation failure and poor weather conditions, they may also contain large gaps between data points. Since we must be able to compute continuum flux at any given time, we have to employ a suitable interpolation method. Although linear interpolation between data points is the simplest way to achieve this task, it does not resolve intraday variability. Furthermore, it does not account for any uncertainty associated with the interpolation process or data points. Therefore, we use a stochastic model of AGN variability to interpolate between the continuum data points and extrapolate them into the future and past beyond the duration of reverberation mapping campaign. This has the added benefit of providing a way to incorporate uncertainty of interpolation into our analysis and propagate the uncertainty into the inference of BLR properties.

6.1 Method

6.1.1 Gaussian Processes

Here we adapt our discussion on Gaussian Processes based on the discussion provided in Rasmussen & Williams (2006) Chapter 2.2. A Gaussian Process (GP), which is specified by a mean function

and a covariance matrix C, is defined as a collection of random variables, any finite subset of which has a joint Gaussian distribution. Here we model AGN continuum light curve as a GP. Unlike a parametric approach, which defines the dependent variable y as a function of the independent variable t with a fixed number of parameters, a GP approach does not specify the number of parameters involved upfront. Rather, it considers all the functions f(t) that are consistent with available data. Therefore, the term non-parametric does not mean there are no parameters; quite the contrary. It means we do not limit the number of parameters (i.e. there are infinitely many parameters). To set our prior for the functions, we start by considering the time domain we are interested in. Selecting a time interval to include few days both preceding and following data is a logical choice. The functions are further constrained by the data: a time series of continuum flux values $\{y\} = (y_1, y_2, \ldots, y_n)$ measured consecutively at n different instances in time $\{t\} = (t_1, t_2, \ldots, t_n)$. That is, we only consider functions which lie within the specified domain in time, and, which go through all the data points $\{y\}$. Therefore, these data points are also called *training points*. Our goal is to evaluate flux values at $\{f_*\} = (f_{*1}, f_{*2}, \ldots, f_{*n_*})$ at n_* instances in time $\{t*\} = (t_{*1}, t_{*2}, \ldots, t_{*n_*})$, which are named *test points*. With GP assumption, our prior distribution for any finite set of these interpolated fluxes $\{f_*\}$ is a multivariate Gaussian

$$\mathbf{f}_* \sim \mathcal{N}(\boldsymbol{\mu_*}, K_{**}) \tag{6.1}$$

with joint probability density given by,

$$p(\mathbf{f}_*|\boldsymbol{\mu_*}, K_{**}) = \frac{1}{\sqrt{(2\pi)^{n_*}\det\ K_{**}}}\ \exp\ \left(-\frac{1}{2}(\mathbf{f}_* - \boldsymbol{\mu_*})^T K_{**}^{-1}(\mathbf{f}_* - \boldsymbol{\mu_*})\right) \tag{6.2}$$

where,

$\boldsymbol{\mu*}$ - mean vector of the interpolated fluxes (or long-term mean).

K_{**} - symmetric, positive definite, $n_* \times n_*$ covariance matrix which evaluates the similarity of *test points* to each other.

The covariance matrix ensures that input time values that are close together will produce output flux values that are close together. The covariance between interpolated fluxes is given by a positive definite kernel function

$$cov(f_{*i}, f_{*j}) = k(t_{*i}, t_{*j}) = \sigma^2\ \exp\ \left[-\left(\frac{|t_{*i} - t_{*j}|}{\tau}\right)^{\alpha}\right] \tag{6.3}$$

where,

t_{*i} and t_{*j} - any two points in time of the interpolated continuum, of which we want to calculate the covariance.

σ - long-term standard deviation of the continuum light curve.

τ - typical time scale of variations. (This is equivalent to damping time scale in DRW).

α - a smoothing parameter between 1 and 2.

Real observed data have associated uncertainties in measurement. Incorporating this noise, the prior on the noisy observations is given by,

$$\mathbf{y} \sim \mathcal{N}(\boldsymbol{\mu}, K + {\sigma_n}^2 I) \tag{6.4}$$

where,

$\boldsymbol{\mu}$ - mean vector of the measured fluxes {y}.

K - $n \times n$ covariance matrix which evaluates the similarity of *training points* to each other.

${\sigma_n}^2$ - variance of the Gaussian noise distribution $\{\epsilon\}$ of data {y}.

The covariance of the data points are given by,

$$cov(f_i, f_j) = k(t_i, t_j) + {\sigma_n}^2 \delta_{ij} \tag{6.5}$$

where,

δ_{ij} - Kronecker delta which is one for i = j, and zero for i $\neq$ j.

We take μ and μ_* to be zero for simplicity. Since {y} and $\{f_*\}$ are taken to be GPs, the joint prior distribution of our *training points* and *test points* is given by,

$$\begin{bmatrix} \mathbf{y} \\ \mathbf{f}_* \end{bmatrix} \sim \mathcal{N}\left(\mathbf{0}, \begin{bmatrix} K + \sigma_n^2 I & K_* \\ {K_*}^T & K_{**} \end{bmatrix} \right) \tag{6.6}$$

where,

K_* - $n \times n_*$ covariance matrix which evaluates the similarity of *training points* to *test points*.

${K_*}^T$ - $n_* \times n$ covariance matrix which is the transpose of K_*.

We can obtain the posterior distribution over the functions by restricting this joint prior distribution to have only the functions which agree with our data $\{t_i, y_i\}$. This could be achieved by

conditioning the joint Gaussian prior on the observations to yield the key predictive equations of GP regression

$$\mathbf{f}_*|\mathbf{t},\mathbf{y},\mathbf{t}_* \sim \mathcal{N}(\bar{\mathbf{f}_*}, cov(\mathbf{f}_*)) \tag{6.7}$$

where,

$$\bar{\mathbf{f}_*} \triangleq \mathbb{E}\left[\mathbf{f}_*|\mathbf{t},\mathbf{y},\mathbf{t}_*\right] = {K_*}^T\left[K+\sigma_n^2 I\right]^{-1}\mathbf{y} \tag{6.8}$$

$$cov(\mathbf{f}_*) = K_{**} - {K_*}^T\left[K+\sigma_n^2 I\right]^{-1}K_* \tag{6.9}$$

We can sample $\mathbf{f}_*$ at $\mathbf{t}_*$ by calculating the mean and the covariance matrix from equations 6.8 and 6.9 respectively.

6.1.2 Cholesky Decomposition

Cholesky decomposition factorizes a symmetric, positive definite matrix into a product of lower triangular matrix L and its transpose upper traiangular matrix L^T.

$$\left[K+\sigma_n^2 I\right] = LL^T \tag{6.10}$$

Calculating inverse of a square matrix could be numerically unstable and therefore computing Cholesky factor L is considered a more robust method. Also, it is a more computationally efficient method.

Using Cholesky factorization in equation 6.9,

$$\begin{aligned} cov(\mathbf{f}_*) &= K_{**} - {K_*}^T\left[LL^T\right]^{-1}K_* \\ &= K_{**} - {K_*}^T(L^T)^{-1}L^{-1}K_* \\ &= K_{**} - (L\backslash K_*)^T(L\backslash K_*) \\ &= K_{**} - V^TV \end{aligned} \tag{6.11}$$

where we have used $V = L\backslash K_*$ (i.e. $LV = K_*$).

Using this in equation 6.8,

$$\begin{aligned} \bar{\mathbf{f}_*} &= (LV)^T\left[LL^T\right]^{-1}\mathbf{y} \\ &= V^TL^T(L^T)^{-1}L^{-1}\mathbf{y} \\ &= V^T(L\backslash\mathbf{y}) \end{aligned} \tag{6.12}$$

With these simplifications, we can use equations 6.12 and 6.11 to calculate predictive mean and predictive covariance matrix, without inverting matrices.

6.1.3 GP Regression Algorithm

Here we provide an algorithm adapted for our purpose based on the algorithm provided in Rasmussen & Williams (2006) page 19.

---

input : $\boldsymbol{t}$ (inputs), $\boldsymbol{y}$ (targets), k (covariance function), σ_n^2 (noise), $\boldsymbol{t_*}$ (test input)
output: $\bar{f}_*$ (predictive mean), $\mathbb{V}[f_*]$ (predictive variance)

---

1. $L = Cholesky(K + \sigma_n^2 I)$
2. $\mathbf{v} = L \backslash \mathbf{k}_*$
3. $\bar{f}_* = \mathbf{v}^T (L \backslash \mathbf{y})$
4. $\mathbb{V}[f_*] = k(\mathbf{t}_*, \mathbf{t}_*) - \mathbf{v}^T \mathbf{v}$

Algorithm 1: GP Regression

6.2 Code

Summary:

- Programming language: Python
- Version : 2.7.10
- Packages: numpy, pyplot (matplotlib)
- Input:
  - Day - (float array) times at which fluxes were measured $\{t\}$ in days.
  - Flux - (float array) measured fluxes $\{y\}$ in arbitrary units.
  - FluxError - (float array) Uncertainity in flux measurements $\{\epsilon\}$ in arbitrary units.
- Variables (changeable within the program):
  - Hyperparameters (depends on the given AGN):
    - tau - (float) characteristic time scale of variability τ in days.
    - alpha - (float) smoothing parameter α between 1 & 2.
  - Other variables:

    * filename - (string) specifies the input file name.
    * nstar - (int) determines how densly the interpolated light curve sampled.
    * a - (non-negative float) determines the amount of extrapolation.

- Output:
  - mu - (float array) mean $\bar{f}_*$ of the interpolated fluxes.
  - fstar - (float array) 5 sample interpolated curves f_* drawn from posterior.
  - varfstar (float array) variance $\mathbb{V}[f_*]$ of interpolated fluxes.

This program implements algorithm 1 and interpolates and extrapolates AGN continuum light curves obtained from reverberation mapping campaigns. It assumes that the input data (time, flux, and uncertainty in flux measurements) are stored in a file in that order. The user has the option to choose which continuum light curve to use by specifying the variable filename. Once the filename is specified, the program reads the data from that specific file. There is also the option to extrapolate the light curve beyond the duration of campaign both before the start date and after the end date by giving a non-zero positive value for parameter a. For example, setting a = 0.5 will result in a light curve extrapolated 50% the continuum data range beyond the end points. Variable nstar determines how many points the specified time range be divided into, for calculating fluxes. Hyperparameters tau and alpha lets the user choose the time scale of the variations and the smoothing parameter between I and 2 respectively. (see Discussion for more details).

```
### Program to interpolate and extrapolate AGN continuum light curves using GP
    regression ###
import numpy as np
import matplotlib.pyplot as plt

### Generate the covariance matrix ###
def cov(a,b):
  ab = np.zeros((len(a), len(b)))
  for i in range(len(a)):
    for j in range(len(b)):
      ab[i][j] = SIGMA2 *np.e**(-((abs(a[i]-b[j]))/tau)**alpha)
  return ab

```

```
### Import data ###
filename = "Arp151_Vband.txt"
with open(filename) as f:
    data = f.read()
data = data.split('\n')

### Input (i.e. Training points / Data) ###
# {t}
Day = np.array([float(row.split('\t')[0]) for row in data]).reshape(-1,1)
# {y}
Flux = np.array([float(row.split('\t')[3]) for row in data]).reshape(-1,1)
# {e}
FluxError = np.array([float(row.split('\t')[4]) for row in data]).reshape
    (-1,1)

mean = np.mean(Flux)
flux = Flux - mean
# variance of the flux error vector
sigma2_n = np.var(FluxError)
# variance of the flux vector
SIGMA2 = np.var(Flux)

### Hyperparameters (Depends on characteristics of the given AGN) ###
# time scale of variations in days
tau = 70.
# smoothing parameter between 1 & 2
alpha = 1.5

### Other ariables ###
# number of test points
nstar = 1001
# fraction of the Data range to extrapolated
a = 0.5

### Set the range ###
# starting Day
```

```
tstarmin = int(round(((1+a)*Day[0]-a*Day[-1])))
# end Day
tstarmax= int(round(((1+a)*Day[-1]-a*Day[0])))

### Test points ###
# {t*}
DayStar = np.linspace(tstarmin, tstarmax, nstar).reshape(-1,1)

### covariance matrices ###
# K
K = cov(Day, Day)
# K*
K_star = cov(Day, DayStar)
# K**
Kstar_star = cov(DayStar, DayStar)

### Cholesky Decomposition ###
# L = Cholesky(K + sigman^2 I)
L = np.linalg.cholesky(K + sigma2_n*np.eye(len(Day)))
# v = (L\K*)
v = np.linalg.solve(L, K_star)

### predictive mean ###
# E[f*]
mu = mean + np.dot(v.T, np.linalg.solve(L, flux)).reshape((nstar,))

### predictive variance ###
# k** - v^2
varfstar = np.diag(Kstar_star) - np.sum(v**2, axis=0)
# stdv of fstar
stdv = np.sqrt(varfstar)

### Draw samples from the posterior at our test points. ###
L = np.linalg.cholesky(Kstar_star - np.dot(v.T, v))
fstar = mu.reshape(-1,1) + np.dot(L, np.random.normal(size=(nstar,5)))

```

```
ymin, ymax = min(mu)-1.5*max(stdv), max(mu)+1.5*max(stdv)

plt.figure()
plt.errorbar(Day, Flux, yerr = FluxError, fmt = 'k.')
plt.plot(DayStar, fstar)
plt.gca().fill_between(DayStar.flat, mu-2*stdv, mu+2*stdv, color="#dddddd")
plt.plot(DayStar, mu, 'r--')
plt.axis([tstarmin, tstarmax, ymin, ymax])
plt.title('Samples from the GP posterior')
plt.show()
```

Listing 6.1: Continuum Interpolation

6.3 Discussion

Here we have implemented a Gaussian Processes regression method in Python to produce interpolated continuum light curves from observed data with associated uncertainties.
If there are no uncertainties in measurement, such as in the case of simulated data, the noise level will be zero. Then, from equation 6.4 the prior on noise-free observations become,

$$\mathbf{y} \sim \mathcal{N}(\boldsymbol{\mu}, K) \tag{6.13}$$

Similarly, the covariance function from equation 6.5 and the covariance matrix of the joint prior distribution from equation 6.6 will be modified as follows.

$$cov(f_i, f_j) = k(t_i, t_j) \tag{6.14}$$

$$\begin{bmatrix} \mathbf{y} \\ \mathbf{f}_* \end{bmatrix} \sim \mathcal{N}\left(\mathbf{0}, \begin{bmatrix} K & K_* \\ {K_*}^T & K_{**} \end{bmatrix} \right) \tag{6.15}$$

Therefore, our new predictive equations for the noise-free case are given by,

$$\bar{\mathbf{f}_*} \triangleq \mathbb{E}\left[\mathbf{f}_* | \mathbf{t}, \mathbf{y}, \mathbf{t}_*\right] = {K_*}^T \left[K\right]^{-1} \mathbf{y} \tag{6.16}$$

$$cov(\mathbf{f}_*) = K_{**} - {K_*}^T \left[K\right]^{-1} K_* \tag{6.17}$$

For simplicity, we have set the value of μ to be zero. However, this is not the case for real observed data. Therefore, we subtract the mean value from observed fluxes and use this mean-subtracted flux values for our calculations. Once we have obtained the predictive mean from the

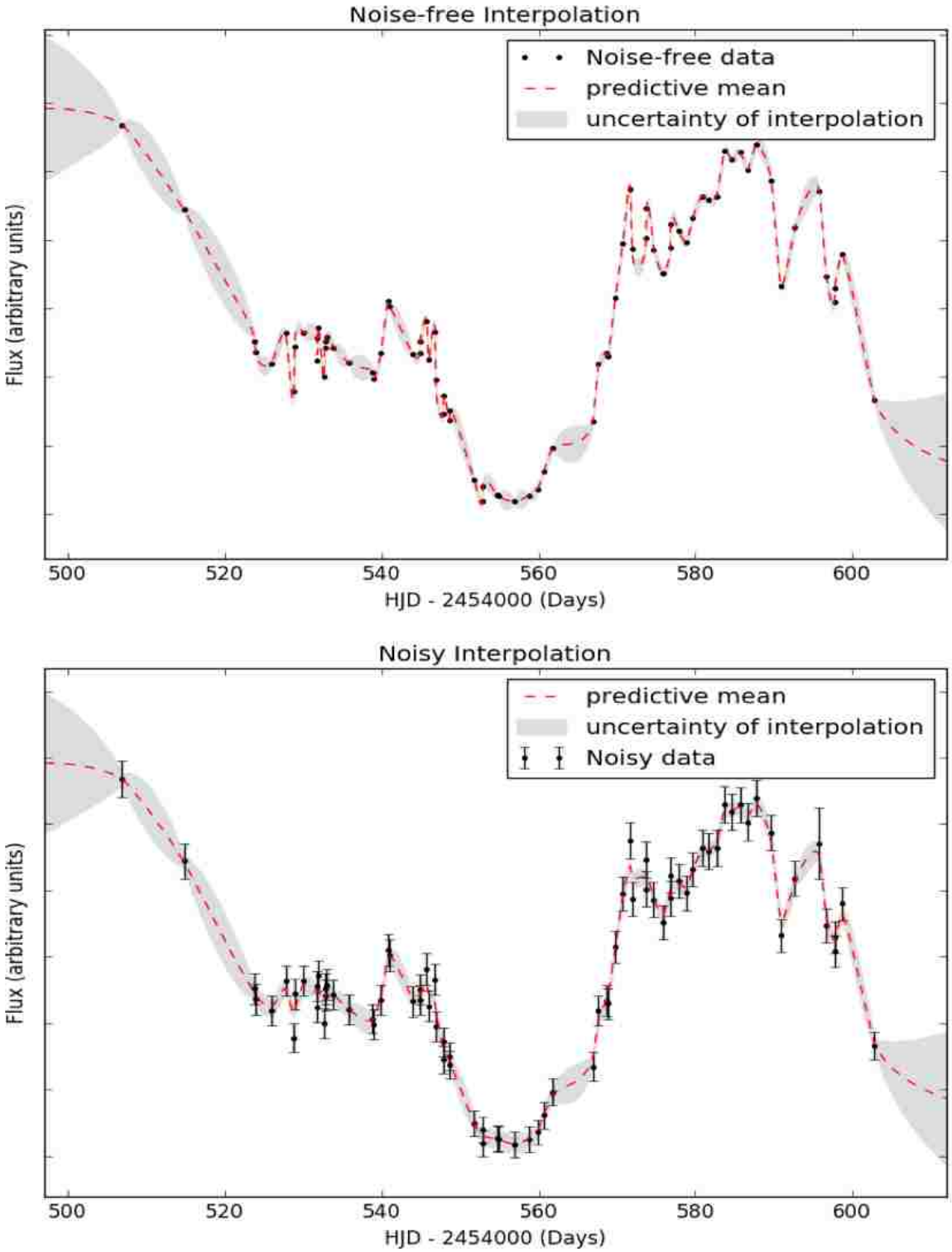

Figure 6.1: Plots illustrating the difference between the interpolation of noise-free data and noisy data using Arp151 V-band continuum observations from LAMP 2008 dataset. Hyperparameters used are $(\tau, \alpha) = (60, 1.4)$.

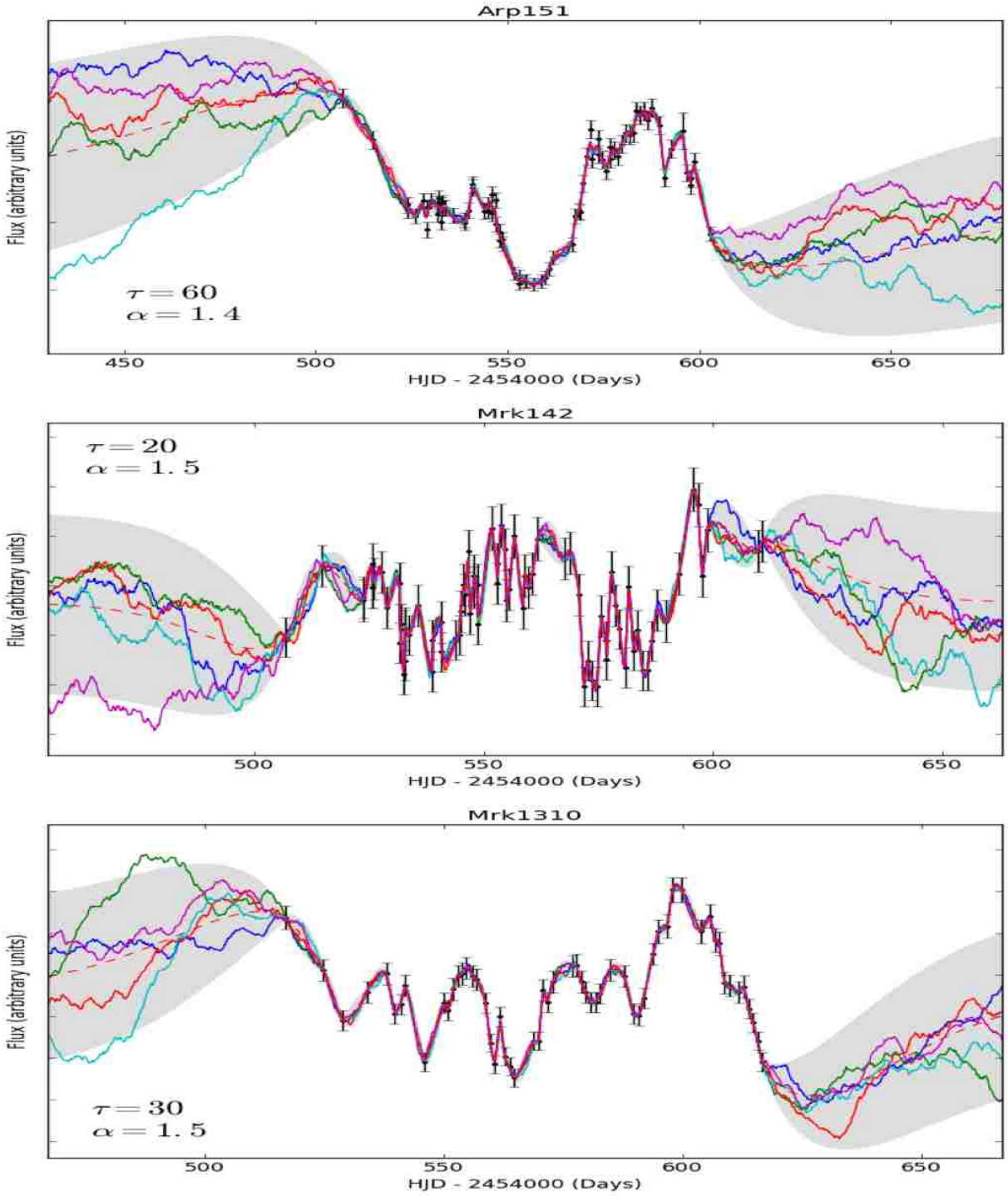

Figure 6.2: Interpolated and extrapolated light curves of three objects from the LAMP 2008 dataset. Black dots with error bars represent the observed data. Red dashed line is the predictive mean of the interpolated fluxes. Solid lines are five samples drawn from the posterior distribution representing five different realizations of the interpolated continuum. The grey area is the 95% confidence interval. Light curves are extrapolated by 50% of the duration beyond the extremities of the data.

calculations, we add the subtracted mean to the predictive mean, thus correcting the offset created by this process. This method works because both observed fluxes and mean-subtracted fluxes have the same variance.

Notice that the uncertainty in interpolated fluxes does not depend on the data $\{y\}$ in equations 6.9 and 6.17. However, it does depend on the variance of the uncertainty of data $\{\epsilon\}$, as one would expect. A larger variance in uncertainty will result in a larger predictive variance. Also noteworthy is the fact that the farther the input values are from data points, the larger the uncertainty becomes. This effect is especially evident in the extrapolated portions beyond the end points of dataset. This is because there are no further data to constrain the prediction.

The program 1 can be used for interpolating both noisy data and noise-free data. Setting the uncertainty in measurement to zero (i.e. FluxError = 0 in the program) will yield results for the noise-free case.

Figure 6.1 shows the difference between interpolated light curves of noise-free data and noisy data using the same data and hyperparameters in both cases. Notice that in the noise-free case, the predictive mean function goes through the exact data points while that of noisy data does not, for the same values of hyperparameters.

Figure 6.2 shows several interpolated and extrapolated continuum light curves from Lick AGN Monitoring Project 2008 dataset (LAMP; Walsh et al. (2009); Bentz et al. (2009)) along with hyperparamters used in creating them.

Although our covariance function should yield a positive-definite matrix theoretically, it does not always happen due to limitations in floating-point number representation in computers. In such instances, we can ensure it becomes at least positive semi-definte by adding a small value to the diagonal of the matrix. Its best to start with a small value for the jitter and lower its value until we reach the smallest value which produces at least a positive semi-definite matrix (i.e. such that the diagonal elements will become non-negative). This is important because if the jitter is comparable to the data, it will act as the noise and will alter the results.

Hyperparameters are the free parameters in covariance function. Their values are determined by the timescales and levels of variability of the AGN which produced light curve data. Determining values of σ_n is straightforward since it is simply the uncertainty of data. In the absence of any additional information, it is reasonable to assume σ is the standard deviation of the available data {y}. Although it is customary to use the term long-term standard deviation this term could be misleading. While it is completely reasonable to assume this within the duration of a campaign,

combining data of multiple campaigns for the same object to produce a single standard deviation value across data sets is unwise. It is a well established fact (Peterson et al. (2002)) that some AGN undergo highly active and relatively inactive periods over timescales of years giving rise to breathing effect. In such occasions the flux variances for different campaigns may differ considerably.

Figures 6.3 and 6.4 show the effects of changing hyperparameters: characteristic time scale τ and smoothing parameter α. The hyperparameter τ determines how long we need to move along the input time axis for the function values to become uncorrelated. This point is reached sooner if the value of τ is lower as evidenced by the top panel of by figure 6.3. A very large value of τ will cause the covariance to become almost independent of the input. This practically removes the input from the inference. The hyperparameter α determines the smoothness of the function. The larger the α, more correlated are the interpolated fluxes, resulting in less fluctuations in small time scales. If we set α to be 1, the GP model becomes equivalent to a CAR(1) process.

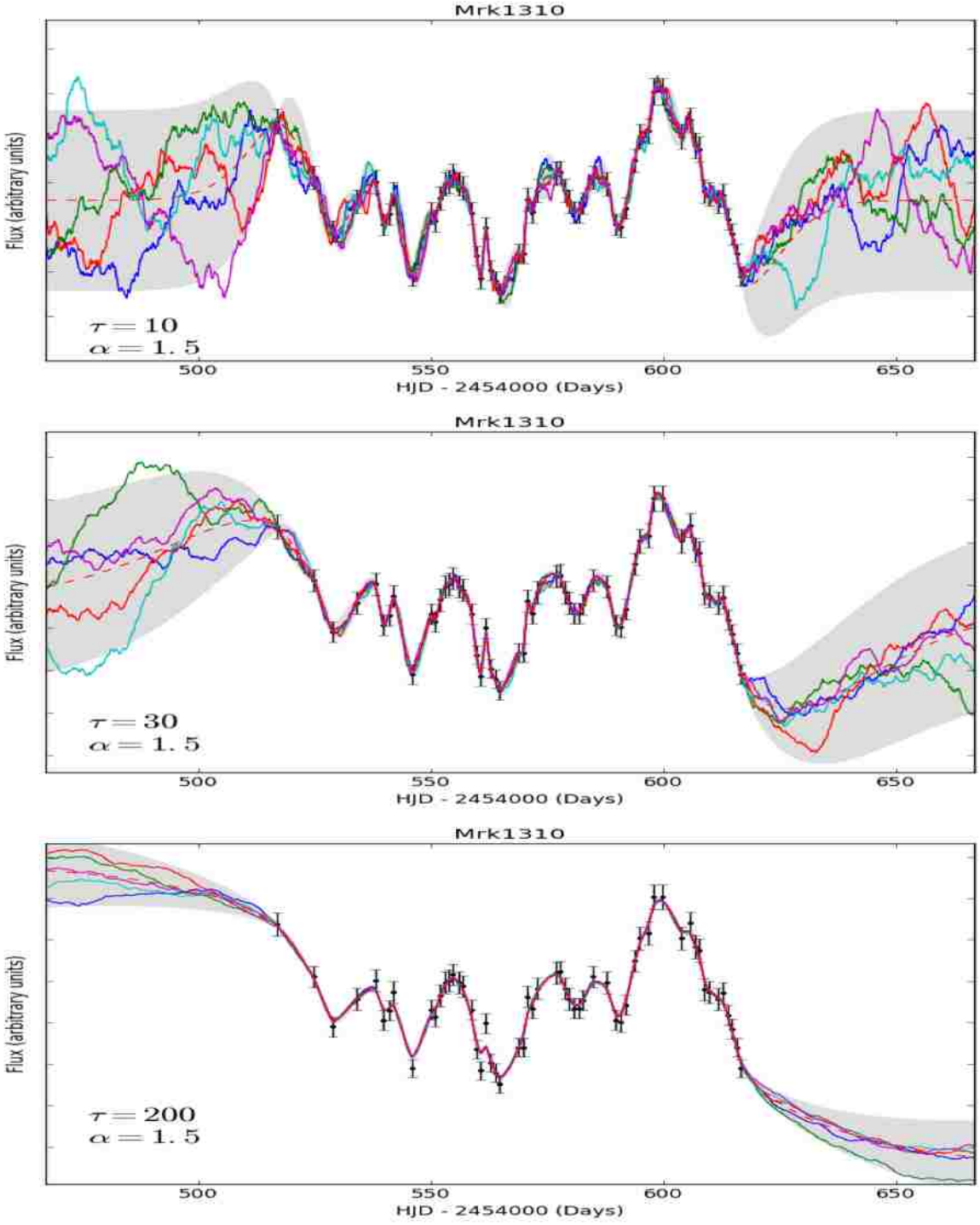

Figure 6.3: Effect of changing hyperparameter τ for the same data
Black dots with error bars represent the observed data. Red dashed line is the predictive mean of the interpolated fluxes. Solid lines are five samples drawn from the posterior distribution representing five different realizations of the interpolated continuum. The grey area is the 95% confidence interval. Light curves are extrapolated by 50% of the duration beyond the extremities of the data.

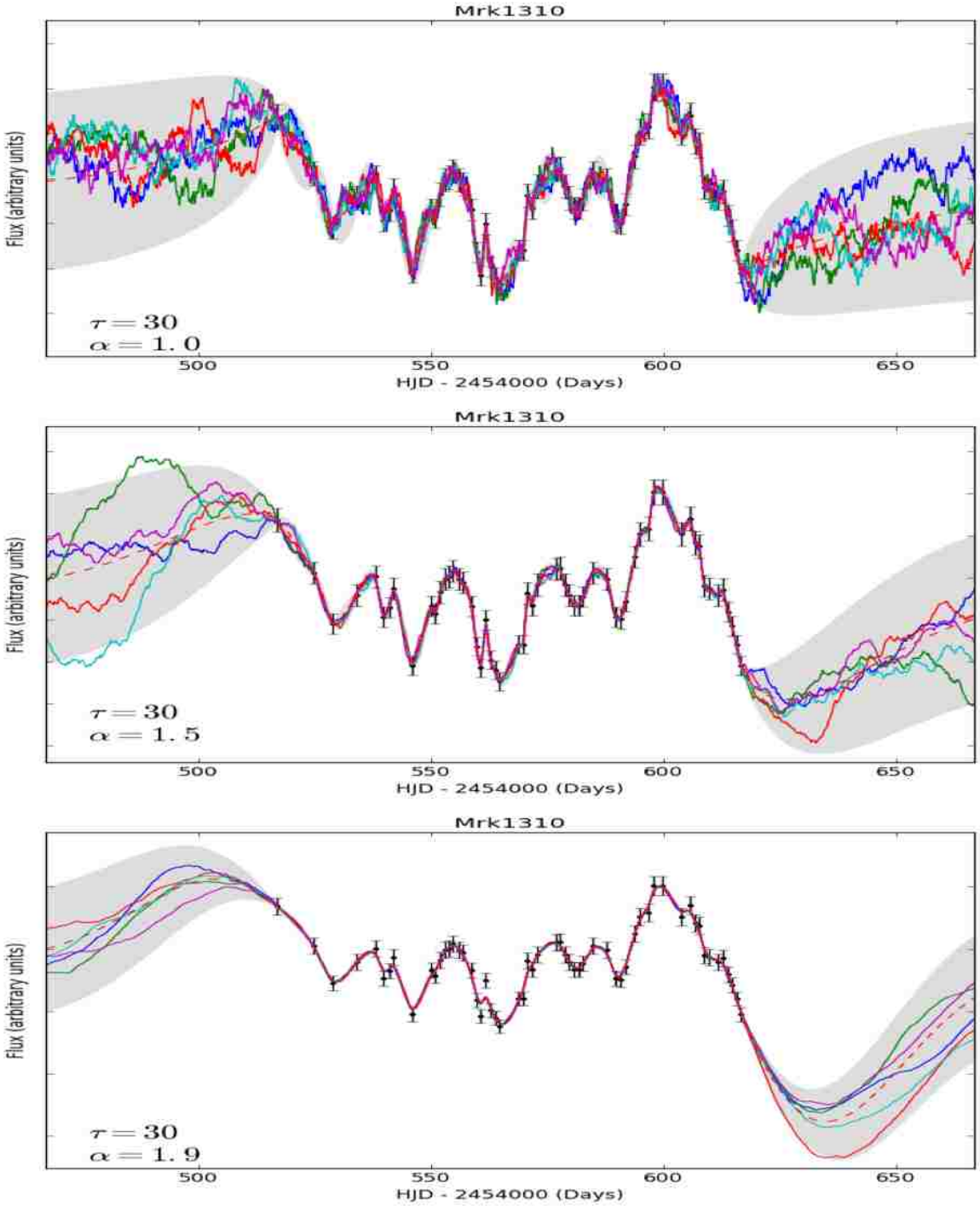

Figure 6.4: Effect of changing hyperparameter α for the same data
Black dots with error bars represent the observed data. Red dashed line is the predictive mean of the interpolated fluxes. Solid lines are five samples drawn from the posterior distribution representing five different realizations of the interpolated continuum. The grey area is the 95% confidence interval. Light curves are extrapolated by 50% of the duration beyond the extremities of the data.

Chapter 7

Future Prospects

A natural next step for this work would be to increase the number of parameters constrained in the disk-wind model of the BLR. Since this would require higher dimension parameter space exploration, using computationally efficient methods is crucial. Therefore, employing more efficient methods rather than grid methods, such as nested sampling or diffusive nested sampling is a logical path to take. Also, we can extend this method to other more sophisticated models of BLR such as hydrodynamical line driven disk winds such as the one described in Proga & Kallman (2004). Finally, we can test the validity of such models by exploring them real reverberation mapping data interpolated using th method described in Chapter 6.

Bibliography

Alexander, T., & Netzer, H. 1994, MNRAS, 270, 781

—. 1997, MNRAS, 284, 967

Andrillat, Y., & Souffrin, S. 1968, Astrophys. Lett., 1, 111

Antonucci, R. R. J., & Cohen, R. D. 1983, ApJ, 271, 564

Arav, N., Barlow, T. A., Laor, A., & Blandford, R. D. 1997, MNRAS, 288, 1015

Arav, N., Barlow, T. A., Laor, A., Sargent, W. L. W., & Blandford, R. D. 1998, MNRAS, 297, 990

Arav, N., Li, Z.-Y., & Begelman, M. C. 1994, ApJ, 432, 62

Bahcall, J. N., Kozlovsky, B.-Z., & Salpeter, E. E. 1972, ApJ, 171, 467

Baldwin, J. A., Ferland, G. J., Korista, K. T., Hamann, F., & Dietrich, M. 2003, ApJ, 582, 590

Barth, A. J., Bennert, V. N., Canalizo, G., et al. 2015, ApJS, 217, 26

Bentz, M. C., & Katz, S. 2015, PASP, 127, 67

Bentz, M. C., Walsh, J. L., Barth, A. J., et al. 2009, ApJ, 705, 199

—. 2010, ApJ, 716, 993

Blandford, R. D., & McKee, C. F. 1982, ApJ, 255, 419

Blumenthal, G. R., & Mathews, W. G. 1975, ApJ, 198, 517

Bottorff, M. C., Korista, K. T., Shlosman, I., & Blandford, R. D. 1997, in Astronomical Society of the Pacific Conference Series, Vol. 113, IAU Colloq. 159: Emission Lines in Active Galaxies: New Methods and Techniques, ed. B. M. Peterson, F.-Z. Cheng, & A. S. Wilson, 215

Brewer, B. J., Treu, T., Pancoast, A., et al. 2011, ApJL, 733, L33

Burbidge, E. M. 1967, ARA&A, 5, 399

Chiang, J., & Murray, N. 1996, ApJ, 466, 704

Clavel, J., Reichert, G. A., Alloin, D., et al. 1991, ApJ, 366, 64

Collin-Souffrin, S., Alloin, D., & Andrillat, Y. 1973, A&A, 22, 343

Corbin, M. R. 1997, ApJ, 485, 517

Courvoisier, T. J.-L., & Clavel, J. 1991, A&A, 248, 389

Denney, K. D., Peterson, B. M., Dietrich, M., Vestergaard, M., & Bentz, M. C. 2009, ApJ, 692, 246

Denney, K. D., Peterson, B. M., Pogge, R. W., et al. 2010, ApJ, 721, 715

Dietrich, M., Wagner, S. J., Courvoisier, T. J.-L., Bock, H., & North, P. 1999, A&A, 351, 31

Du, P., Hu, C., Lu, K.-X., et al. 2014, ApJ, 782, 45

Du, P., Lu, K.-X., Hu, C., et al. 2016a, ApJ, 820, 27

Du, P., Lu, K.-X., Zhang, Z.-X., et al. 2016b, ApJ, 825, 126

Dumont, A. M., & Collin-Souffrin, S. 1990a, A&A, 229, 313

—. 1990b, A&AS, 83, 71

Emmering, R. T., Blandford, R. D., & Shlosman, I. 1992, ApJ, 385, 460

Eracleous, M., & Halpern, J. P. 1994, ApJS, 90, 1

—. 2003, ApJ, 599, 886

Ferland, G. J., & Mushotzky, R. F. 1982, ApJ, 262, 564

Fromerth, M. J., & Melia, F. 2000, ApJ, 533, 172

Gilbert, A. M., Eracleous, M., Filippenko, A. V., & Halpern, J. P. 1999, in Astronomical Society of the Pacific Conference Series, Vol. 175, Structure and Kinematics of Quasar Broad Line Regions, ed. C. M. Gaskell, W. N. Brandt, M. Dietrich, D. Dultzin-Hacyan, & M. Eracleous, 189

Goad, M., & Wanders, I. 1996, ApJ, 469, 113

Goad, M. R., Korista, K. T., & Ruff, A. J. 2012, MNRAS, 426, 3086

Graham, A. W., Onken, C. A., Athanassoula, E., & Combes, F. 2011, MNRAS, 412, 2211

Grier, C. J., Peterson, B. M., Pogge, R. W., et al. 2012a, ApJL, 744, L4

—. 2012b, ApJ, 755, 60

Grier, C. J., Martini, P., Watson, L. C., et al. 2013, ApJ, 773, 90

Grier, C. J., Trump, J. R., Shen, Y., et al. 2017, ArXiv e-prints, arXiv:1711.03114

Hamann, F., & Ferland, G. 1999, ARA&A, 37, 487

Hu, C., Du, P., Lu, K.-X., et al. 2015, ApJ, 804, 138

Ivezić, Ž., & MacLeod, C. 2014, in IAU Symposium, Vol. 304, Multiwavelength AGN Surveys and Studies, ed. A. M. Mickaelian & D. B. Sanders, 395–398

Jackson, N., Perez, E., & Penston, M. V. 1991, MNRAS, 249, 577

Kaspi, S., Maoz, D., Netzer, H., et al. 2005, ApJ, 629, 61

Kaspi, S., Smith, P. S., Netzer, H., et al. 2000, ApJ, 533, 631

Kelly, B. C., Bechtold, J., & Siemiginowska, A. 2009, ApJ, 698, 895

Korista, K. T., & Goad, M. R. 2000, ApJ, 536, 284

Korista, K. T., Alloin, D., Barr, P., et al. 1995, ApJS, 97, 285

Kozłowski, S., Kochanek, C. S., Udalski, A., et al. 2010, ApJ, 708, 927

Krolik, J. H. 1988, ApJ, 325, 148

Li, Y.-R., Wang, J.-M., Ho, L. C., Du, P., & Bai, J.-M. 2013, ApJ, 779, 110

MacLeod, C. L., Ivezić, Ž., Kochanek, C. S., et al. 2010, ApJ, 721, 1014

Mathews, W. G. 1986, ApJ, 305, 187

Mathews, W. G., & Capriotti, E. R. 1985, in Astrophysics of Active Galaxies and Quasi-Stellar Objects, ed. J. S. Miller, 185–233

McConnell, N. J., & Ma, C.-P. 2013, ApJ, 764, 184

Murray, N., & Chiang, J. 1997, ApJ, 474, 91

Murray, N., Chiang, J., Grossman, S. A., & Voit, G. M. 1995, ApJ, 451, 498

Netzer, H. 1990, in Active Galactic Nuclei, ed. R. D. Blandford, H. Netzer, L. Woltjer, T. J.-L. Courvoisier, & M. Mayor, 57–160

Netzer, H. 2013, The Physics and Evolution of Active Galactic Nuclei

Onken, C. A., Ferrarese, L., Merritt, D., et al. 2004, ApJ, 615, 645

Pancoast, A., Brewer, B. J., & Treu, T. 2011, ApJ, 730, 139

—. 2014, MNRAS, 445, 3055

Park, D., Kelly, B. C., Woo, J.-H., & Treu, T. 2012, ApJS, 203, 6

Pastoriza, M., & Gerola, H. 1970, Astrophys. Lett., 6, 155

Peterson, B. M. 1993, PASP, 105, 247

Peterson, B. M. 2001, in Advanced Lectures on the Starburst-AGN, ed. I. Aretxaga, D. Kunth, & R. Mújica, 3

Peterson, B. M. 2006, in Lecture Notes in Physics, Berlin Springer Verlag, Vol. 693, Physics of Active Galactic Nuclei at all Scales, ed. D. Alloin, 77

—. 2008, NewAR, 52, 240

Peterson, B. M., Meyers, K. A., Carpriotti, E. R., et al. 1985, ApJ, 292, 164

Peterson, B. M., Wagner, R. M., Crenshaw, D. M., et al. 1983, AJ, 88, 926

Peterson, B. M., & Wandel, A. 1999, ApJL, 521, L95

—. 2000, ApJL, 540, L13

Peterson, B. M., Berlind, P., Bertram, R., et al. 2002, ApJ, 581, 197

Peterson, B. M., Ferrarese, L., Gilbert, K. M., et al. 2004, ApJ, 613, 682

Proga, D., & Kallman, T. R. 2004, ApJ, 616, 688

Proga, D., Stone, J. M., & Drew, J. E. 1999, MNRAS, 310, 476

Proga, D., Stone, J. M., & Kallman, T. R. 2000, ApJ, 543, 686

Rasmussen, C. E., & Williams, C. K. I. 2006, Gaussian Processes for Machine Learning

Rokaki, E., Boisson, C., & Collin-Souffrin, S. 1992, A&A, 253, 57

Schimoia, J. S., Storchi-Bergmann, T., Nemmen, R. S., Winge, C., & Eracleous, M. 2012, ApJ, 748, 145

Schimoia, J. S., Storchi-Bergmann, T., Winge, C., Nemmen, R. S., & Eracleous, M. 2017, ArXiv e-prints, arXiv:1708.03727

Shields, G. A. 1976, ApJ, 204, 330

—. 1977, Astrophys. Lett., 18, 119

Sivia, D. S., & Skilling, J. 2006, Data analysis: a Bayesian tutorial

Storchi-Bergmann, T., Nemmen da Silva, R., Eracleous, M., et al. 2003, ApJ, 598, 956

Strateva, I. V., Strauss, M. A., Hao, L., et al. 2003, AJ, 126, 1720

Sulentic, J. W., Marziani, P., Zamanov, R., et al. 2002, ApJL, 566, L71

Tohline, J. E., & Osterbrock, D. E. 1976, ApJL, 210, L117

Trakhtenbrot, B., & Netzer, H. 2012, MNRAS, 427, 3081

Ulrich, M.-H., Boksenberg, A., Penston, M. V., et al. 1991, ApJ, 382, 483

Vanden Berk, D. E., Richards, G. T., Bauer, A., et al. 2001, AJ, 122, 549

Véron-Cetty, M.-P., Véron, P., & Gonçalves, A. C. 2001, A&A, 372, 730

Walsh, J. L., Minezaki, T., Bentz, M. C., et al. 2009, ApJS, 185, 156

Waters, T., Kashi, A., Proga, D., et al. 2016, ApJ, 827, 53

Welsh, W. F., & Horne, K. 1991, ApJ, 379, 586

Woo, J.-H., Treu, T., Malkan, M. A., Ferry, M. A., & Misch, T. 2007, ApJ, 661, 60

Curriculum Vitae

Graduate College

University of Nevada, Las Vegas

Champika Sandamali Weerasooriya

Degrees:

Bachelor of Science in Physics 2007

University of Peradeniya, Sri Lanka

Master of Science in Physics 2012

University of Kentucky, Lexington

Dissertation Title: Probing Broad Line Regions of Active Galactic Nuclei

Dissertation Examination Committee:

Chairperson, Dr. George Rhee, Ph.D.

Committee Member, Dr. Daniel Proga, Ph.D.

Committee Member, Dr. Stephen Lepp, Ph.D.

Graduate Faculty Representative, Dr. David Lee, Ph.D.